INTERNATIONAL JOURNAL OF ENERGY STUDIES

e-ISSN: 2717-7513 (ONLINE); homepage: https://dergipark.org.tr/en/pub/ijes

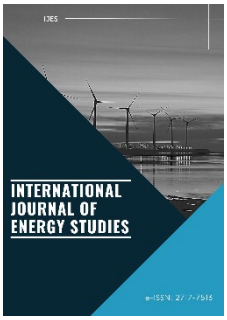

Research Article
Int J Energy Studies 2024; 9(4): 679-721
DOI: 10.58559/ijes.1570736

Received : 20 Oct 2024
Revised : 18 Nov 2024
Accepted : 20 Nov 2024

Evaluating machine learning techniques for fluid mechanics: Comparative analysis of accuracy and computational efficiency

Eyup Kocak*

**Cankaya University, Mechanical Engineering Department, Ankara, 06790, Türkiye, ORCID: 0000-0002-1544-2579*
*(*Corresponding Author:eyupkocak@cankaya.edu.tr:)*

Highlights

- The study evaluates the effectiveness of different machine learning methods, such as artificial neural network, random forest, and support vector machine, in solving fluid mechanics problems.
- After parameter optimization, machine learning techniques achieved R^2 values above 0.9 in multiple cases, outperforming numerical methods in predictive accuracy.
- The study found that Linear Regression does not effective for selected fluid mechanics problems, while other machine learning methods performed well after optimization.
- In cases with limited data, artificial neural networks outperformed other machine learning models, suggesting its robustness in scenarios with constrained datasets.

You can cite this article as: Kocak E. Evaluating machine learning techniques for fluid mechanics: Comparative analysis of accuracy and computational efficiency. Int J Energy Studies 2024; 9(4): 679-721.

ABSTRACT

This study focuses on applying machine learning (ML) techniques to fluid mechanics problems. Various ML techniques were used to create a series of case studies, where their accuracy and computational costs were compared, and behavior patterns in different problem types were analyzed. The goal is to evaluate the effectiveness and efficiency of ML techniques in fluid mechanics and to contribute to the field by comparing them with traditional methods. Case studies were also conducted using Computational Fluid Dynamics (CFD), and the results were compared with those from ML techniques in terms of accuracy and computational cost. For Case 1, after optimizing relevant parameters, the Artificial Neural Network (ANN), Random Forest (RF), and Support Vector Machine (SVM) models all achieved an R^2 value above 0.9. However, in Case 2, only the ANN method surpassed this threshold, likely due to the limited data available. In Case 3, all models except for Linear Regression (LR) demonstrated predictive abilities above the 0.9 threshold after parameter optimization. The LR method was found to have low applicability to fluid mechanics problems, while SVM and ANN methods proved to be particularly effective tools after grid search optimization.

Keywords: Fluid mechanics, Solar dryer, Artifical neural networks, Converging-diverging nozzle, Stirrer

1. INTRODUCTION

Fluid mechanics significantly impacts our daily lives, encompassing phenomena such as water and airflow, as well as conduction and convection problems. One notable application is in irrigation systems, where fluid mechanics principles optimize water resource utilization effectively and efficiently [1]. In agriculture, these principles help maintain soil moisture and facilitate plant watering. The design and analysis of such systems often rely on a combination of computational fluid dynamics (CFD) and experimental methods [2].

Problem-solving in fluid mechanics typically employs a combination of experimental, numerical, and analytical methods. While experimental studies are valuable, they often involve high costs and significant time requirements. Additionally, working with prototype dimensions can introduce errors, necessitating the reduction of problems to model scale. Technological advancements have increased the use of CFD simulations, offering a more efficient alternative to experimental studies. However, CFD simulations can also be time-consuming and require substantial computing power, potentially introducing numerical errors, especially for inexperienced designers. Analytical methods are only applicable to a limited range of problems. In recent decades, machine learning (ML) methods are made progress in fluid mechanics problems. The main advantages of using ML techniques in fluid mechanics are given as follows:

- Machine learning techniques can use massive amounts of data in order to solve the problem. ML algorithms can analyze the data set more powerfully than traditional techniques.
- Machine learning methods can introduce flexible algorithms for nonlinear CFD problems.
- Machine learning can leverage high-performance computers through parallel computing and distributed processing capabilities, allowing it to effectively utilize large datasets. This enables faster solving of fluid mechanics problems and provides the opportunity to obtain more comprehensive results.
- ML techniques can also be used in optimization problems. Algorithms can evaluate the different combinations and serve the best scenario for the problem.

ML techniques are gradually applied to reduced-order modeling, reconstruction and prediction, turbulence model closure, flow control techniques, and optimization problems. The usage of ML in fluid mechanics goes deep. In 1950s, Rosenblatt [3], designed expert systems that think like human brain. Minsky and Papert [4], dampened the initial excitement of ML, they claimed that a single-layer linear perceptron's inability to solve the Exclusive OR (XOR) problem. As a result,

the progress of neural network development experienced a significant setback. In 1986, Hinton et al. [5], proposed a new learning procedure called as the backpropagation algorithm and LeCun et al [6], used this method successfully in the recognition of handwritten zip code digits. In 1984, Mehta and Kutler [7], applied artificial intelligence to computational aerodynamics. They concluded that expert systems will be a valuable tool, especially for tackling aerodynamic tasks. Indeed, when examining the studies conducted from those days to the present, it is evident that this statement has been confirmed by numerous research endeavors.

In today's world, machine learning techniques have established themselves as a prominent source of data with satisfactory accuracy and power in the field of renewable energy. In the study of Aziz [8] the prediction of renewable energy in India is predicted with using hybrid machine learning methods. The predictions are compared with the methods that are currently used and it is seen that ML model is a powerful tool in forecasting energy. Sakthi et al. [9] proposed ML technique for renewable energy analysis based on photovoltaic cell for wind energy hybridization. They used convolutional kernel support regression vector as a ML method and it is shown that the ML method can predict building energy demand and supply. Tirth et al. [10] used ML methods to predict the energy production for smart grid-based energy storage system. The prediction ability of the techniques used is 99% when compared with the experimental results. Li and Yi [11] used artificial neural networks (ANN) and genetic algorithms (GA) to optimize the geometrical parameters of the shell pavilion and maximize energy generation instead of using a time-consuming numerical approach. They found an optimal design by using this technique instead of the convolutional methods.

Aerospace applications have also emerged as another application area of machine learning techniques. In recent years, machine learning has been extensively applied in aerodynamics, leading to successful outcomes. Li et al [12], reviewed several researches that uses machine learning method to optimize the aerodynamic shape of the airfoil. In sight of the review it is observed that ML can handle with the big training data sets achieving high prediction accuracy in the aerodynamic coefficients also, can contribute new optimization architectures to address the limitations of numerical techniques. Zan et al. [13], tried convolutional neural network (CNN) to aerodynamic shape optimization. They define 109 input parameters as angle of attack, Mach number, chord length, wing span...etc. They examined the effect of CNN parameters in the predictive performance. It is seen that CNN parameters directly affects the accuracy therefore

before starting to the optimization with ML techniques, the parameters of the selected ML model should be optimized for each of the problem. Peng et al. [14] utilized CNN for predict the airfoil lift coefficients. CNN achieves 0.97% error while regression models have error rate of 10%. Khan et al. [15] applied CNN for compressible flow jet with circular ribs. They investigate the effect of the diameter, location of the rib also the nozzle geometry. In their ANN algorithm they used Mach number, rib diameter, rib location as an input while the output parameters are pressure loss and power. They compared the prediction ability of ANN, CNN and Deep Neural Network (DNN) models. They claimed that CNN predicted the wall pressure data with the highest accuracy.

Lastly, an exemplification of the successful application of ML techniques can be observed in the domain of ventilation, where endeavors are made to optimize flow patterns, predict air quality, and enhance the performance of ventilation systems. In a study by Esrafilian-Najafabadi and Haghighat [16], various prediction models were investigated to anticipate the performance of air-conditioning systems. Decision trees, k-nearest neighbors (kNN), multi-layer perceptron, and gated recurrent units were implemented to tackle the aforementioned problem. Notably, the kNN method was utilized, whereby an exhaustive search was conducted, exploring numerous potential combinations within a defined range, often referred to as the grid search technique. This approach facilitated the exploration of a multitude of optimization possibilities within a relatively short span of time.

As mentioned above, the applicability of ML techniques to fluid mechanics problems is progressively increasing day by day. Furthermore, the success of ML methods is noted to exhibit significantly higher levels of accuracy compared to traditional approaches. Ulucak et al. [17] showed that in the optimization process of the geometrical parameters of the solar chimney power plant to maximize the power output, the most important advantage of soft computing techniques, when compared with numerical methods, is the drastic reduction of computational costs. Also in several researches, it is showed that root mean square error (RMSE) values are drastically reduced with the machine learning techniques [18]–[20]. In Table 1, some of the studies are summarized that uses ML techniques for different fluid mechanics and heat transfer problems.

Table 1. Several literatures uses ML techniques in fluid mechanics & heat transfer problems

Authors	Specific Problem	Results
Ayli and Kocak [19]	Heat transfer in pipes with twisted tape is predicted with ANN	R^2 is 0.97043, higher accuracy, less time than CFD
Sim et al [21]	the piston bowl geometry and injector design with CFD and ML techniques	ML design provided similar performance at mid-load but a 3.8–4.5 % reduction in fuel consumption compared to the base design
Aly and Clarke [22]	CFD and ML techniques are used for the wind design of solar panels	ML can speed up 10.000 times faster than CFD & more efficient design is obtained with ML
Ye and Hsu [23]	structural fire response prediction with numerical and ML techniques	Higher accuracy with Random Forest and Gradient Boosting models in real-time displacement prediction
Jin et al. [24]	Finding the influence of nasal vestibule structure on nasal obstruction with Ml method	The ML results are verified by the cooperation of clinical means with a high accuracy level.
Le at al. [25]	Efficiency enhancement of Cyclone separators with deep learning	k-fold cross-validation is utilized. DL approach decreases the computational cost while increasing the accuracy level.
Milicevic et al. [26]	Random Forest, Gradient Boosting and Artificial Neural Networks are used to predict the biomass trajectories of particle mass burnout.	ANN showed the best predictions for both particle mass burnout with higher R^2 values.
Upadhyay et al. [27]	prediction of the CFB riser axial solid holdup profile with the ANN method	ML model produces more output data than experiments with low computational cost and higher accuracy
Nasution et al. [28]	the pressure of convective water flow within a copper metal foam tube prediction with ANFIS	Using the GAFIS and ANFIS algorithms, a lot of computational time could be saved compared to the CFD calculation time

This study focuses on applying machine learning (ML) techniques to fluid mechanics problems and introduces a novel approach by integrating ML methods with computational fluid dynamics simulations for performance evaluation and optimization. The objective is to assess the effectiveness and efficiency of ML techniques in solving fluid mechanics problems while contributing to advancements in this field through systematic comparisons with traditional CFD methods. To achieve this, three distinct fluid mechanics problems—flow around a covering-diverging nozzle, flow in a vortex mixer, and flow in a solar dryer—were selected as case studies. Initial numerical analyses, numerical verifications and geometric optimizations were conducted

using ANSYS Fluent to generate robust datasets. These datasets were then utilized to implement and optimize various ML methods, including artificial neural networks (ANN), support vector machines (SVM), and regression learners.

The study focuses on two different aims. First, high-quality data for ML training is generated through validated CFD simulations; second, ML techniques are systematically compared in terms of accuracy and computational efficiency across different fluid mechanics problems. By examining the behavior of ML methods under varying problem conditions and with limited parameter datasets, the study aims to provide insights into the practical applicability and reliability of these techniques. The findings emphasize the potential of ML methods to reduce computational costs significantly while maintaining high prediction accuracy, offering a compelling alternative to traditional numerical approaches.

2. NUMERICAL STUDIES

2.1. Case I: Flow In A Vortex-Mixer

2.1.1. Problem description

Stirring is crucial for fluid mechanics problems like mixing, precipitation, dissolution, and chemical reactions. The failure of the efficient mixing can even cause the complete failure of the process. Mixing intensity relies on the impeller type, number of blades of the impeller, shaft location, and arrangement of internals. In the design process of the mixer, optimization of the blade geometry is one of the crucial steps. In this part of the study, the geometrical parameter effect on the stirrer efficiency is investigated.

The geometry of the stirrer tank is depicted in Figure 1. The ratio of stirrer diameter to vortex mixer diameter (*d/D*) and fluid height to vortex mixer diameter (*h/D*) varies between 0.4 to 0.6 and 0.5-0.8, respectively. The rotational speed range is $4.16<\omega<16.6$. The effect of the stirrer diameter, initial liquid height and rotational speed on the shape of the vortex by examining the *z/h*, tangential and axial velocity is investigated. The shaft holds the impeller, which has two blades and is located concentric to the axis of the tank.

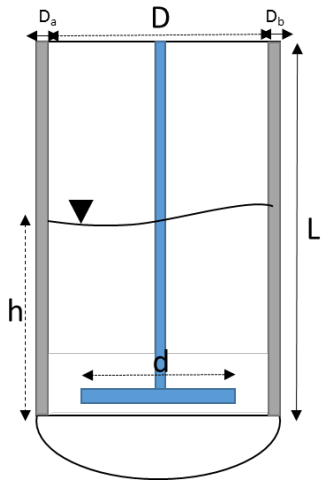

(a)

(b)

Case	d/D	h/D	Ω (rps)
Case 1-4	0.4	0.5	4.16,8.3,12.5,16.6
Case 5-8	0.6	0.5	4.16,8.3,12.5,16.6
Case 9-12	0.85	0.5	4.16,8.3,12.5,16.6
Case 13-16	0.6	0.8	4.16,8.3,12.5,16.6
Case 17-20	0.6	0.8	4.16,8.3,12.5,16.6
Case 21-24	0.6	0.8	4.16,8.3,12.5,16.6

Figure 1. (a) Schematic view of the vortex mixer (b) Test cases of the vortex mixer

2.1.2. Numerical methodology

A systematic approach is utilized for the three-dimensional, incompressible, inviscid, and transient problem using the commercial software ANSYS Fluent. The equations governing the flow are given in Eq. (1) and (2) in the Cartesian coordinate system using the index notation. Reynolds-averaging approach is used to model the problem.

$$\frac{\partial \rho}{\partial t} + \frac{\partial}{\partial x_i}(\rho u_i) = 0 \tag{1}$$

$$\frac{\partial(\bar{u}_i)}{\partial t} + \frac{\partial}{\partial x_j}\left(\bar{u}_i \bar{u}_j\right) = -\frac{1}{\rho}\frac{\partial p}{\partial x_i} + \vartheta \frac{\partial}{\partial x_j}\left(\frac{\partial u_i}{\partial x_j}\right) - \frac{\partial \tau_{ij}}{\partial x_j} \tag{2}$$

where x_i is the cartesian coordinates in the x-direction, u_i is the instantaneous Cartesian velocity components, t is time, P is pressure and ν is kinematic viscosity. The subgrid-scale stress is defined by $\tau_{ij} = \rho\overline{u_i u_i} - \rho\overline{u_i u_j}$. As a turbulence model, k-ε is used, which is used in similar studies [29], [30]. The mathematical expression of turbulence kinetic energy, denoted with k, and dissipation rate, denoted with ε, is given as follows [29], [30].

$$\frac{\partial}{\partial x_i}(\rho k u_i) = \frac{\partial}{\partial x_j}\left[\left(\mu + \frac{\mu_t}{\sigma_k}\right)\frac{\partial k}{\partial x_j}\right] + G_k + G_b - \rho\varepsilon - Y_M + S_K \tag{3}$$

$$\frac{\partial}{\partial x_i}(\rho\varepsilon u_i) = \frac{\partial}{\partial x_j}\left[\left(\mu + \frac{\mu_t}{\sigma_\varepsilon}\right)\frac{\partial \varepsilon}{\partial x_j}\right] + C_{1\varepsilon}\frac{\varepsilon}{k}(G_k + C_{3\varepsilon}G_B) - C_{2\varepsilon}\rho\frac{\varepsilon^2}{k} + S_\varepsilon \quad (4)$$

In Equation (3) and (4) G_k is the generation of kinetic energy expressed as [29], [30].:

$$G_k = \mu_t\left(\frac{\partial u_i}{\partial x_j} + \frac{\partial u_j}{\partial x_i}\right)\frac{\partial u_i}{\partial x_j} \quad (5)$$

Turbulence kinetic energy generation due to buoyancy is denoted with G_B. Y_M represents the contribution of the fluctuating dilatation in compressible turbulence to the overall dissipation rate. Pressure-velocity coupling is solved using the SIMPLE algorithm. All governing equations were discretized with a second-order upwind scheme finite volume. Turbulence equations were discretized with first-order upwind scheme finite volume.

A no-slip wall boundary condition is applied to the walls of the tank and the stirrer as a boundary condition. The three-dimensional flow domain is discretized using a tetrahedral unstructured mesh. The mesh is refined in the regions around corners and near the blades to capture fine details. To ensure the result is independent from the mesh, a grid sensitivity analysis is conducted. The number of elements is systematically increased, and the impact of the element size on the power number is investigated. If the power number, as defined in Equation (6), remains unchanged with varying mesh densities, it indicates that the grid has reached a state of insensitivity, yielding consistent results [31].

$$N_p = \frac{P}{\rho N^3 d^5} = \frac{2\pi N\tau}{\rho N^3 d^5} \quad (6)$$

where τ is the torque. As given in Figure 2(a), when the number of mesh elements is $8.5\text{x}10^5$ and 10^6, power number variation is below 1.5%. Therefore, taking into account the computational cost, the number of mesh is chosen as 8.5×10^5.

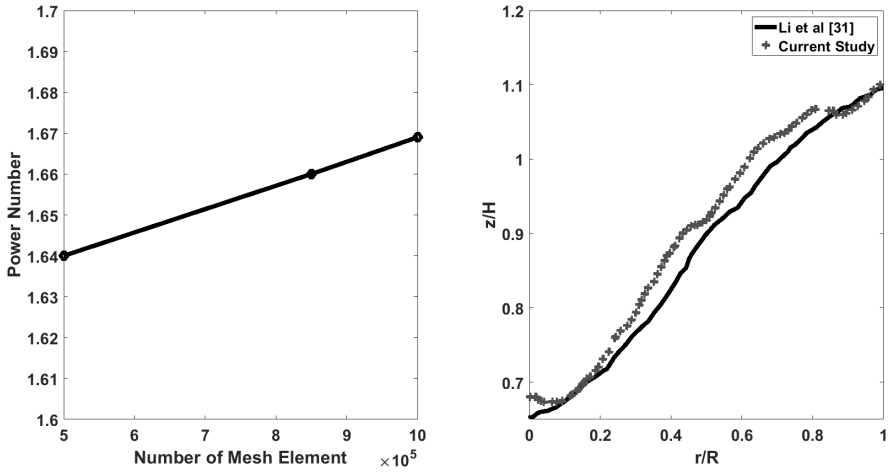

Figure 2. (a) Mesh independency study (b) Validation of the numerical results

To validate the numerical methodology, experimental data from Li et al. [31] is utilized. The specific parameters used in the validation include $H/T = 1$, $D/T = 0.75$, and a stirrer rotation rate of 4.167 rps. The shape of the vortex is determined by employing axial and radial coordinates and generating a polynomial curve, similar to the approach followed in the studies of Li et al.[31] and Sarkar et al. [32]. In Figure 2(b), the obtained vortex shape is compared to the results obtained by Li et al. [31]. The maximum root mean square error (RMSE) is calculated as 9.8%, which is considered satisfactory in terms of agreement between the numerical and experimental results.

2.2. Case II: Solar Air Dryer

2.2.1. Problem description

Solar air dryers offer an environmentally friendly drying method while reducing energy costs by using renewable solar energy. It is widely used especially in the agricultural sector, food industry and industrial drying applications. Solar dryers are mainly used in space heating, agricultural processes, and seasoning, such as timber [33]. The working principle of solar dryers is depicted in Figure 3 (a). Solar air dryers use a collector or solar panels that collect light from the sun, which converts sunlight into thermal energy. The air to be used for the heating process is taken from the outside and transmitted to the dryer through air ducts or fans. The airflow is heated using the thermal energy from the solar panels. This thermal energy transfer occurs while fluid is flowing through the ducts. The heated air passes over the materials in a cyclical flow continuously. In this way, a continuous drying process is carried out. One of the most important factors that directly affect heat transfer is the design of the absorber plate. To enhance the system efficiency, the flow area geometrical modifications are embedded using V-corrugated fins, rectangular fins, or

perforated fins [34], [35]. Therefore, in this part of the study, the effect of the fin on solar air dryer performance is investigated, and data is generated for the machine learning study. The mass flow rate effect and fin spacing effect on performance are investigated.

The investigation focuses on a particular geometry, as illustrated in Figure 3(b). Figure 3(c) provides a detailed representation of the specifications and thermophysical properties associated with the system. The Solar Air Heater (SAH) in question possesses dimensions of 1 m by 0.5 m. Fins are attached to both walls of the SAH, with variations in the number of fins observed across three configurations: 11 fins, 8 fins, and 5 fins.

To comprehensively examine the system's behavior, the mass flow rate is adjusted within the range of 0.01 kg/s to 0.1 kg/s. Each fin configuration is evaluated for multiple mass flow rates, resulting in a total of 15 distinct cases.

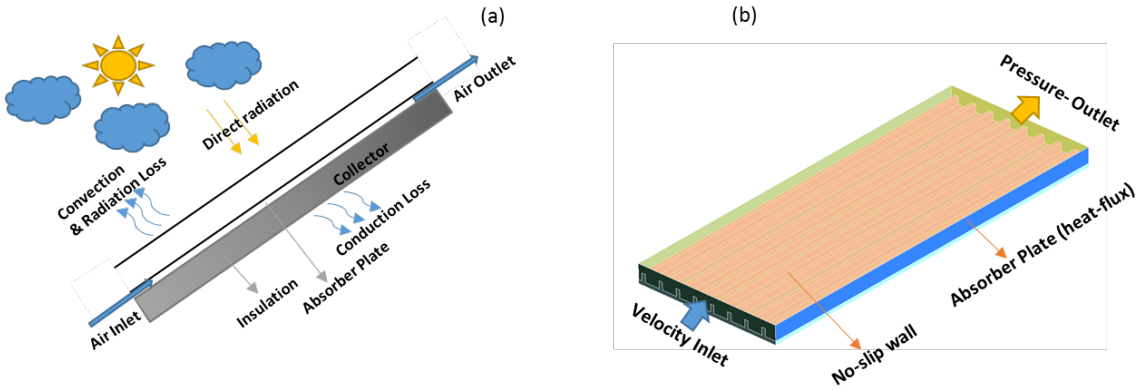

(c)

Property	Air	Glass	Steel
Density (kg/m^3)	1.18	2500	7850
Thermal Conductivity (W/mK)	0.0242	0.81	15
Specific Heat (J/kgK)	1006.43	840	460
Viscosity (Ns/m^2)	1.789E-5	-	-

Figure 3. (a) Schematic view of the solar dryer (b) boundary conditions (c) thermophysical properties

2.2.2. Numerical methodology

The numerical simulation of the solar air dryer is utilized with using ANSYS Fluent software. Continuity, momentum, and energy equation (Eq(1,2)-Eq(7)) are solved for 3-dimensional, steady state, incompressible, and turbulent flow along with the boundary conditions by the finite volume method [36].

$$\rho C_p \left[\frac{\partial T}{\partial t} + (v.\nabla)T\right] = k\nabla^2 T + \emptyset \quad (7)$$

The pressure-velocity coupling is utilized with the SIMPLE algorithm, and the Implicit scheme is used with the hexahedral mesh structure. Pressure, momentum and energy equations are discretized with a second-order upwind scheme. Convergence criteria are set to 10^{-6}. The realizable *k-ε* model was selected to carry out turbulent computation as it produces accurate and satisfactory results according to the studies in the literature [36], [37]. In order to calculate the thermal efficiency of the dryer, the following equation is used [38]:

$$\eta = \frac{Q_u}{A_c I_c} \quad (8)$$

where, A_c is the collector area, and I_c is the global radiation value, which is kept as 882 W/m^2. To calculate the Q_u, Eq (9) is used [39].

$$Q_u = \dot{m} C_p (T_o - T_i) \quad (9)$$

Prior to commencing numerical simulations, a grid sensitivity test was conducted within validation studies for the flat plate dryer. The validation study utilized the experimental work conducted by Karim and Hawlader [39]. Efficiency values were compared for three different flow rates, and the maximum deviation from Karim and Hawlader [39] was found to be at a magnitude of 7.69%. A mesh independence test was conducted based on the efficiency value for a flow rate of 0.01 kg/m^{2}s. At the end of the mesh independence test, it was deemed appropriate to perform the study using 750,000 mesh elements. The comparison of the validation study is presented in Table 2.

Table 2. Validation study regarding to the Karim et al. [39]

Mass Flow rate (kg/m^{2}s)	**Experimental efficiency [39]**	**Current Study efficiency**	**Difference with experimental data [39]**
0.01	0.2743	0.2954	7.69 %
0.04	0.6015	0.6154	2.3 %
0.06	0.6579	0.6785	3.13%

2.3. Case III: Converging-Diverging Nozzle

2.3.1. Problem description

The nozzle, functioning as a mechanical system, serves to regulate the flow direction and enhance the exit velocity of the fluid by effectively harnessing its pressure energy and enthalpy. Converging-diverging nozzles find widespread applications in the design of various systems, including supersonic ramjet or scramjet inlets, internal diffusers, supersonic ejectors, as well as supersonic air-breathing engine inlets, internal diffusers, compressor cascades, and supersonic ejectors. As a result, this system is frequently employed in aerodynamics applications, wherein the cross-sectional area, often rectangular in shape, gradually tapers, resulting in an increase in both pressure and velocity [40], [41].

Figure 4(a) presents a schematic view of the converging-diverging (CD) nozzle. Typically, a pressurized tank is positioned behind the converging section, and the Mach number within the tank is lower than 1. The pressure at the nozzle inlet is referred to as stagnation pressure. Within the tank, the velocity is negligible due to its substantial size. The fluid then flows from the chamber into the converging section of the nozzle, passing through the throat, traversing the diverging section, and ultimately exhausting into the surrounding atmosphere as a jet. Since the primary objective of the CD nozzle is to convert internal energy into kinetic energy and generate thrust, maintaining a high level of uniformity in fluid velocity is crucial and represents one of the most significant design parameters for the nozzle.

The numerical modeling of a converging-diverging (CD) nozzle structure has been conducted as the third case study. The geometry consists of three parts: the converging section, the throat section, and the diverging section. As known from the literature, one of the most influential geometric parameters on nozzle efficiency is the throat angle. Therefore, the exit-to-throat area ratio (AR) has been varied by increments of 0.2 from 1 to 1.6. Another significant parameter is the pressure ratio (NPR), which has been varied in the range of 5 to 10.

Initially, a validation study, including turbulence modeling and time step analysis, was performed based on the governing equations given before. Subsequently, after ensuring the accuracy of the numerical methodology, the effects of the mentioned parameters were investigated.

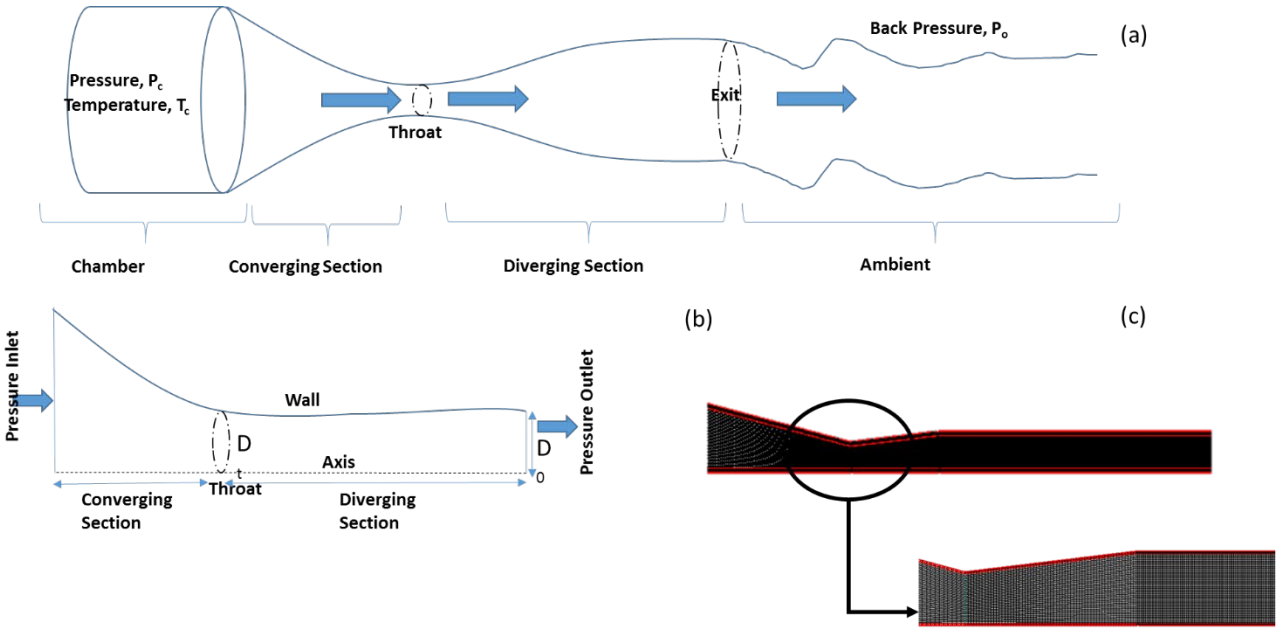

Figure 4. (a) Schematic view of CD Noozle (b) boundary conditions (c) generated mesh structure

2.3.2. Numerical methodology

To analyze compressible flow motion, it is necessary to add one more term, density change in time, to solve the equations of mass, momentum, and energy. These equations are expressed as follows [42]:

$$\frac{\partial \rho}{\partial t} + \frac{\partial}{\partial x_i}(\rho u_i) = 0 \tag{10}$$

$$\frac{\partial}{\partial t}(\rho u_i) + \frac{\partial}{\partial x_j}(\rho u_i u_j) = -\frac{\partial p}{\partial x_i} + \frac{\partial t_{ji}}{\partial x_j} \tag{11}$$

$$\rho \frac{\partial}{\partial t}\left[\rho(e + \frac{1}{2}u_i u_i)\right] + \frac{\partial}{\partial x_j}\left[\rho u_j(\square + \frac{1}{2}u_i u_i)\right] = -\frac{\partial}{\partial x_i}(u_i t_{ij}) + \frac{\partial q_j}{\partial x_j} \tag{12}$$

In these equations, the term "e" represents the internal energy, and "$h = e + p/\rho$" represents the specific enthalpy value. For compressible flows, the term "τ" represents the viscous stress tensor,

which includes the second-order viscosity term and the molecular viscosity term. The boundary conditions that are used to solve governing equations are depicted in Figure 4(b).

The validation phase involved the utilization of data of Mason et al [42] obtained from experiments conducted at the static test facility of Langley's 16-foot transonic tunnel, under identical geometric and flow conditions. Numerical analyses were carried out to compare the computational study with the referenced experimental investigation. The mesh structure was created using the structured approach in the ANSYS Mesh software. Initially, the influence of number of mesh element and size of the mesh on the results is explored. Three distinct mesh structures are considered: coarse, consisting of 750,000 elements; medium, consisting of 1,000,000 elements; and fine, consisting of 2,000,000 elements. Static pressure distributions at the center are plotted for each mesh structure and compared against the experimental data and among themselves. Upon examination of Figure 5, it can be observed that employing a fine mesh structure led to a mere 0.8% enhancement in proximity to the experimental results. Consequently, it is determined that utilizing a medium mesh structure would suffice, as further refinement in the mesh structure did not significantly impact the accuracy of the results, while imposing increased computational costs. Hence, the decision was made to proceed with the medium mesh structure for subsequent analyses. Furthermore, the compliance between the experimental data and numerical simulations, as displayed in the same figure (Figure 5), demonstrated a satisfactory agreement. Finally, the effect of turbulence models on the numerical results was investigated. As depicted in Figure 5 (b), among the three turbulence models examined, the k-epsilon model provided the best approximation. By completing the numerical validation, the study concluded its initial phase, subsequently focusing on investigating the influence of aspect ratio (AR) and nozzle pressure ratio (NPR).

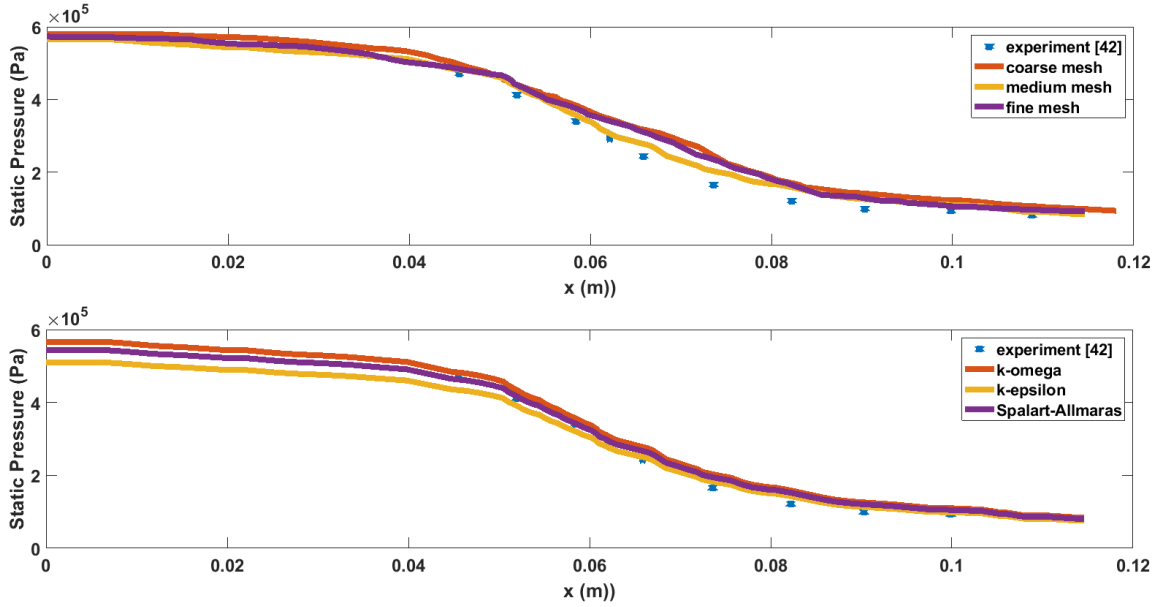

Figure 5. (a) Grid sensitivity test & Validation Study (b) Turbulence model study

3. NUMERICAL RESULTS

3.1. Case I: Flow In A Vortex-Mixer

In this case, the geometrical parameter effect on the stirrer efficiency is investigated. The ratio of stirrer diameter to vortex mixer diameter (*d/D*) and fluid height to vortex mixer diameter (*h/D*) varies between 0.4 to 0.6 and 0.5-0.8, respectively. The rotational speed range is $4.16<\omega<16.6$. The effect of the stirrer diameter, initial liquid height and rotational speed on the shape of the vortex by examining the *z/h*, tangential and axial velocity is investigated. The shaft holds the impeller, which has two blades and is located concentric to the axis of the tank. For each different scenario, vortex shapes were obtained using radial and axial coordinates and generating polynomial curves, as done in the study by Sarkar et al. [32]. Figure 5(a) illustrates the influence of velocity on the vortex shape. It can be observed that as the rotational speed increases, the shear effect intensifies and the vortex structure grows larger. When examining the effect of the *d/D* ratio, it is observed that the impact of the stirrer diameter increases as it approaches the wall edges, while its influence is less dominant in the central region, as seen in Fig 5(b). Increasing the stirrer diameter causes the central vortex to penetrate deeper and leads to an increase in turbulence instabilities. Regarding the initial water level effect, it is clearly seen in Fig 5(c) that it has no effect on the central region. Among the parameters studied, the initial water height is considered to have the least impact.

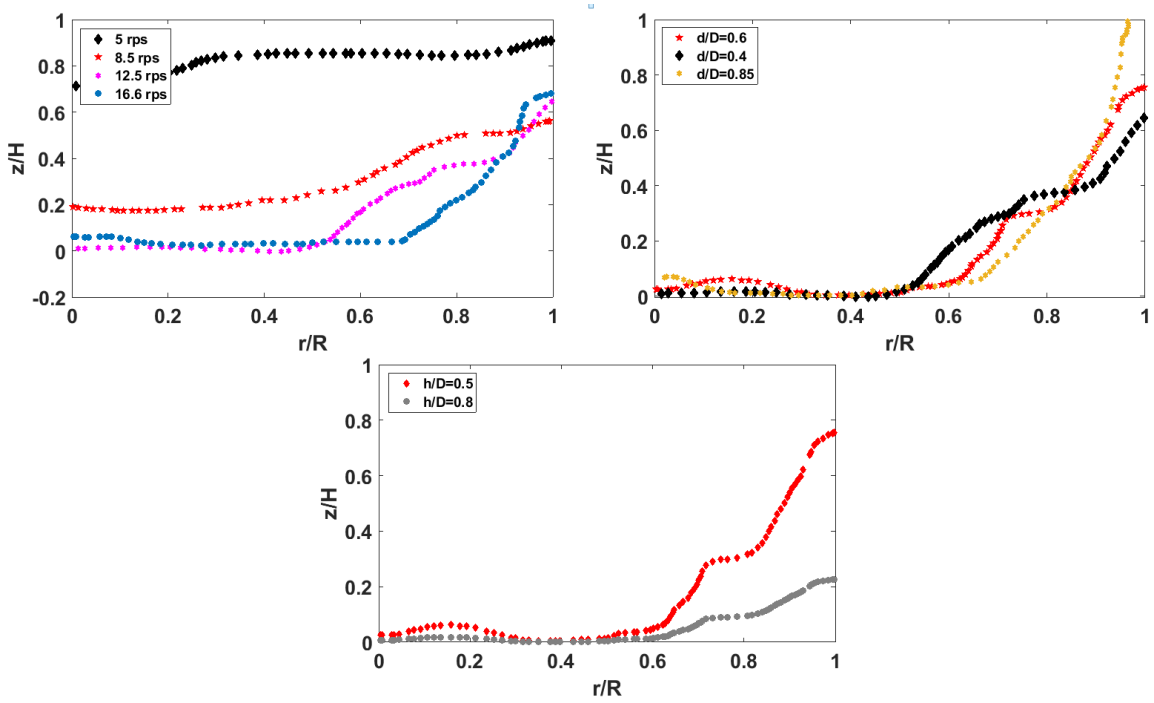

Figure 5. The effect of (a) rps for d/D=0.6 and h/D=0.5, (b) d/D for 12.5 rps and h/D=0.5, (c) h/D for d/D=0.4 and 12.5 rps on the vortex shape.

In Figure 6, radial velocity distributions at different positions are shown. Upon examining the results, it is observed that the velocity initially increases linearly in the radial direction. As it approaches the wall, the velocity gradually rises and then dramatically drops towards zero.

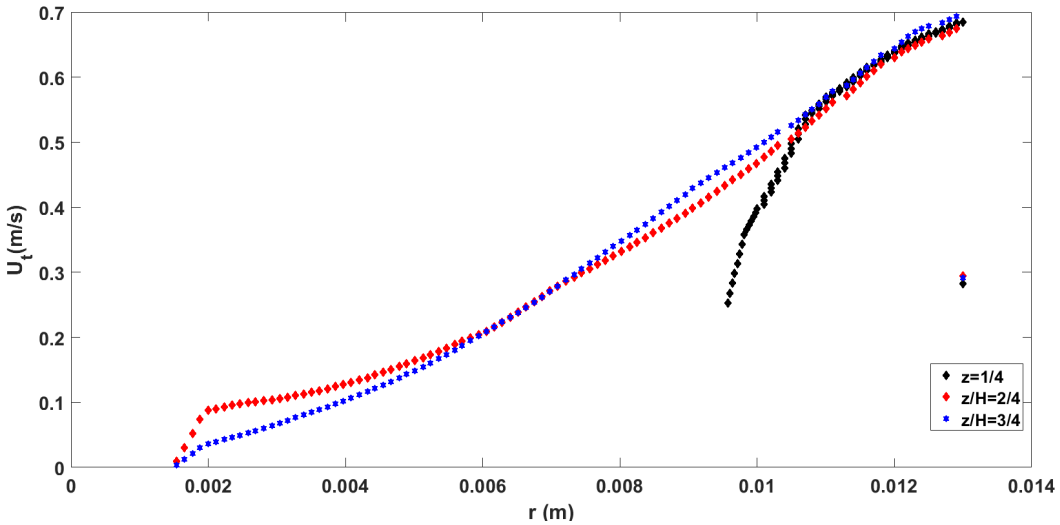

Figure 6. Radial velocity component distribution for D/T=6, h/D=0.5 and 12.5 rps

For different rotational velocities, streamline plots are presented in Figure 7. Symmetrical flow filed is occurred through the shaft of the stirrer. A circulation loop originates above the stirrer. The recirculation zones get larger, and the turbulence intensity increases with the increase in RPM.

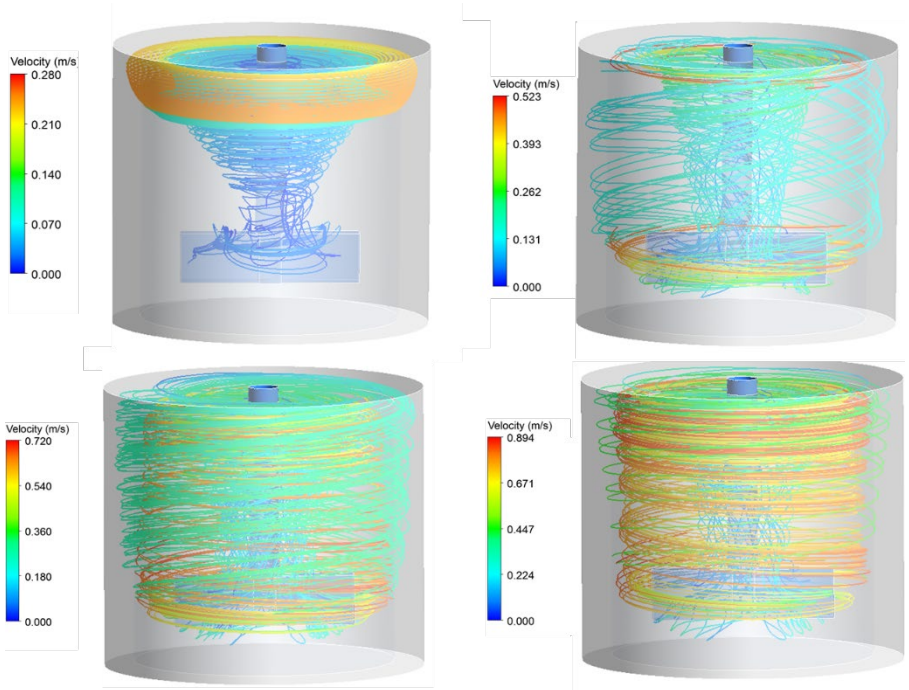

Figure 7. 3-D streamlines for different rotational Phase-I velocities (for *d/D*=0.6 and *h/D*=0.5) (a) 4.16 rps (b) 8.3 rps (c) 12.5 rps (d) 16.6 rps

To observe the effect of the stirrer diameter, velocity contours are plotted on the center plane, as illustrated in Figure 8. It is observed that as the stirrer diameter increases, especially near the tank edges, the velocity values increase. This indicates a stronger vortex structure and a more homogeneous mixing. The vortex energy has also increased with the stirrer diameter.

To observe the effect of the stirrer diameter, velocity contours are plotted on the center plane, as illustrated in Figure 8. It is observed that as the stirrer diameter increases, especially near the tank edges, the velocity values increase. This indicates a stronger vortex structure and a more homogeneous mixing. The vortex energy has also increased with the stirrer diameter.

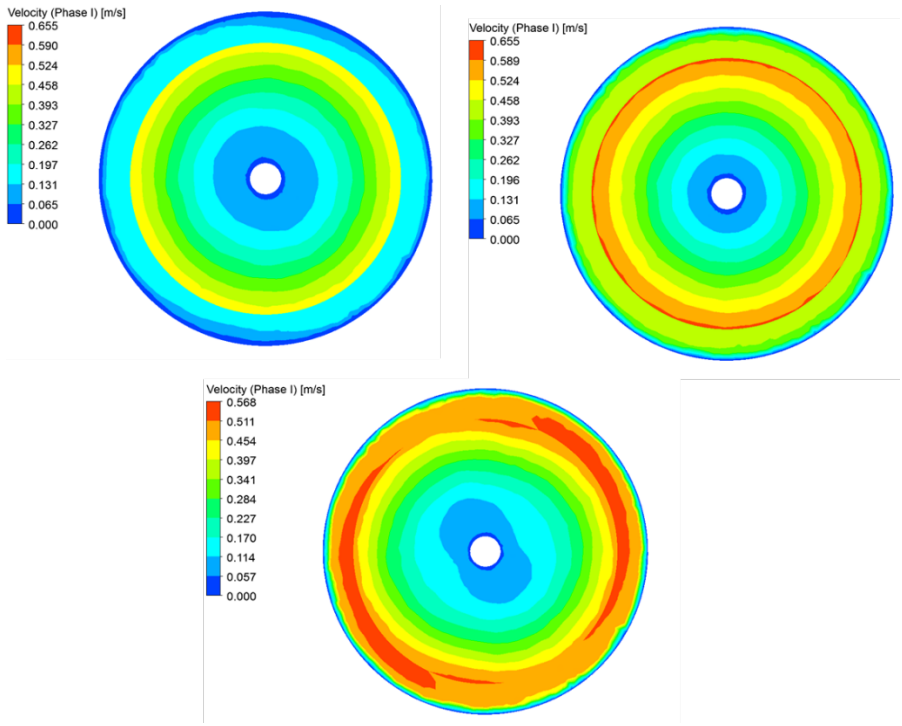

Figure 8. Velocity distribution for different stirrer diameters (a) *d/D*=0.4 (b) *d/D*= 0.6 (c) *d/D*=0.85

3.2. Case II: Solar Air Dryer

The investigation focuses on a particular geometry that provides a detailed representation of the specifications and thermophysical properties associated with the system. The Solar Air Heater has adimensions of 1 m by 0.5 m. Fins are attached to both walls of the SAH, with variations in the number of fins observed across three configurations: 11 fins, 8 fins, and 5 fins. To comprehensively examine the system's behavior, the mass flow rate is adjusted within the range of 0.01 kg/s to 0.1 kg/s. Each fin configuration is evaluated for multiple mass flow rates, resulting in a total of 15 distinct cases.

As the mass flow rate increases, there is an associated increase in the Reynolds number and turbulence, leading to a reduction in the outlet temperature values (Figure 9(a). It is evident from the obtained results that the influence of the mass flow rate is more pronounced at lower flow rates, while its impact on temperature diminishes as the flow rate increases. With the rise in flow rate, thermal efficiency experiences an enhancement due to a decrease in thermal losses as shown in Figure 9(b). Furthermore, it is noteworthy that the effect of the flow rate on efficiency exhibits a more substantial increase of approximately 7% at lower flow rates, whereas at higher flow rates, this influence diminishes to around 3%. However, beyond a critical flow rate, the increased heat transfer to the surrounding environment results in a decline in efficiency. Hence, it can be

concluded that solar dryers possess a critical mass flow rate threshold, whereby exceeding this value leads to a detrimental effect on efficiency.

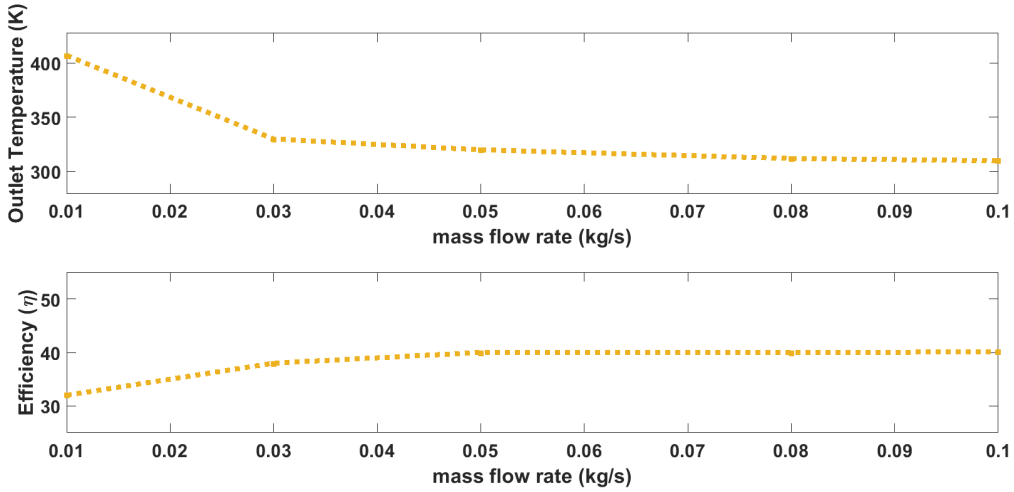

Figure 9. (a)Variation of outlet temperature for different mass flow rates (b) Variation of efficiency for different mass flow rates (n=5)

The impact of fin count on the performance of the solar dryer has been thoroughly investigated, as depicted in Figure 9. It should be noted that the thickness of the fins remained constant throughout the study, while variations in fin count resulted in corresponding changes in fin spacing. Notably, the fin count, particularly at low mass flow rate values (<0.05 kg/s), has exhibited a substantial influence on the efficiency of the system.

A critical observation has been made regarding the relationship between fin spacing and efficiency. As the fin spacing decreases, or, conversely, the fin count increases, it enables improved mixing within the system, leading to increased turbulence and enhanced efficiency. This phenomenon is attributed to the fact that a decrease in fin spacing facilitates better heat transfer through increased surface area, thereby favoring the utilization of closely spaced fins.

The investigation emphasizes the significant role played by fin count in determining the performance of the solar dryer. By optimizing the spacing between fins, the system can achieve improved thermal efficiency through enhanced heat transfer and increased turbulence. The findings underscore the advantage of employing a higher fin count configuration, which facilitates greater surface area for heat transfer and contributes to the overall effectiveness of the solar dryer.

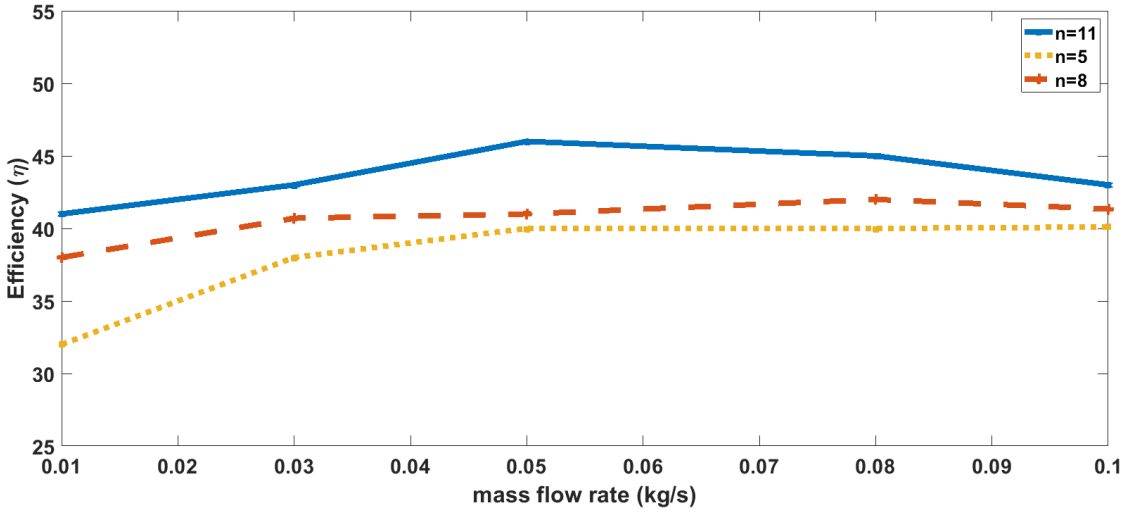

Figure 10. Efficiency variation for different number of fin configurations

Figure 11 presents velocity distributions on seven different planes for varying fin counts. The distribution illustrates the formation of vortex structures within the inter-fin regions. It is evident that as the fin count increases, there is an augmentation in the turbulent kinetic energy and the presence of flow phenomena.

The increasing fin count promotes higher levels of turbulence, leading to intensified fluid motion and enhanced mixing. This phenomenon manifests in the form of vortex structures within the flow field, which contribute to increased turbulence and improved convective heat transfer. The findings highlight the positive influence of higher fin counts on turbulence generation and flow characteristics, indicating a favorable impact on the overall performance of the system.

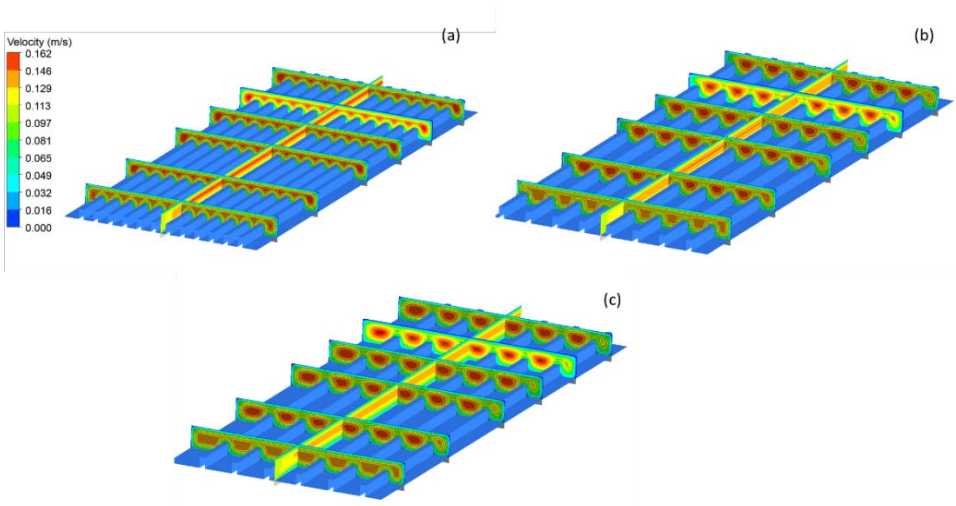

Figure 11. Velocity contour for configuration of (a) 11 fin (b) 8 fin (c) 6 fin

3.3. Case III: Converging-Diverging Nozzle

The numerical modeling of a converging-diverging nozzle structure has been conducted as the third case study. As known from the literature, one of the most influential geometric parameters on nozzle efficiency is the throat angle. Therefore, the exit-to-throat area ratio has been varied by increments of 0.2 from 1 to 1.6. Another significant parameter is the pressure ratio, which has been varied in the range of 5 to 10.

The impact of aspect ratio on temperature and velocity at the exit of the diverging chamber is illustrated in Figure 12. The results clearly demonstrate that the throat area exerts a dominant influence on both velocity and temperature. Specifically, an increase in the AR ratio, corresponding to a reduction in throat diameter, leads to an increase in velocity and thus, volumetric flow rate. Conversely, it has an opposite effect on the exit temperature, causing a decrease. It can be observed that a higher AR value has a positive impact on the generated thrust.

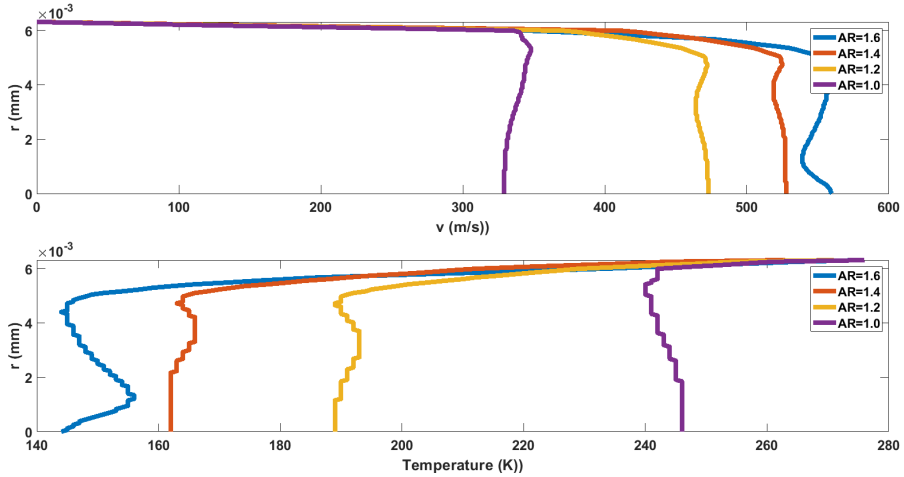

Figure 12. (a) Radial distribution of the tangential velocity at the nozzle exit for different AR values (b) radial distribution of the temperature at the nozzle exit for different AR values

An abrupt increase in the aspect ratio, resulting from a smaller throat diameter, enhances the expansion velocity of the fluid. Consequently, this leads to a greater pressure drop and a subsequent decrease in temperature. As a result, an increase in AR results in an augmentation of flow rate and velocity while concurrently causing a reduction in temperature. Figure 13 presents the turbulence kinetic energy contours for different aspect ratios, highlighting the efficiency of the design. The impact of AR is clearly evident along the walls of the diverging section. As the AR increases, particularly at the nozzle exit, the disturbance in the flow intensifies.

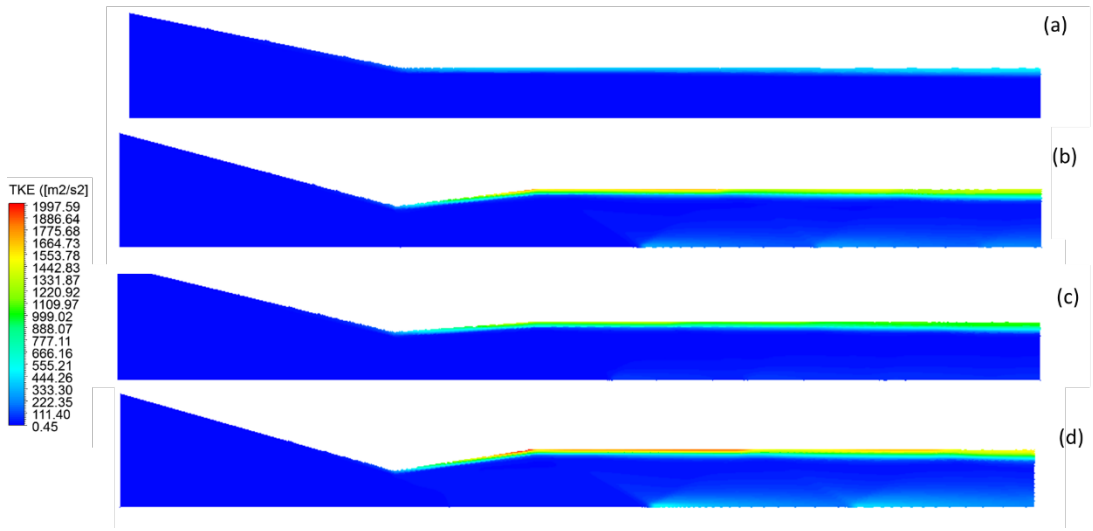

Figure 13. Turbulence kinetic energy distribution through the nozzle (a) AR=1 (b) AR=1.2 (c) AR=1.4 (d) AR=1.6

The effect of varying the inlet pressure on CD nozzle performance was investigated by changing the Nozzle Pressure Ratio (NPR) value in increments of 2 between 5 and 11. The velocity variation at the outlet for different NPR values is shown in Figure 14(a). As observed, the flow reverts to rotational flow in the divergent region especially in the axis, resulting an increase in velocity values. It can be seen that as the NPR value increases, the P_{base} value rises, but the influence of NPR on pressure is more pronounced at lower NPR values.

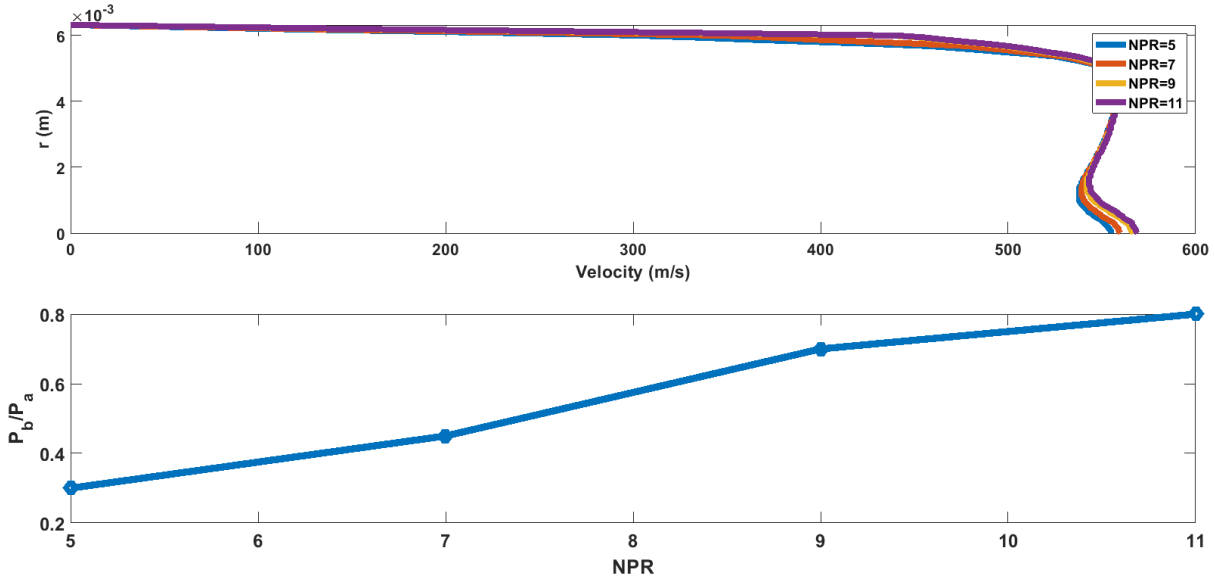

Figure 14. (a) Velocity distribution in the outlet for different NPR values (b) P_b/P_a values at different NPR values

4. MACHINE LEARNING APPROACHES

Machine learning is an artificial intelligence model that generates output based on input data provided by users. ML techniques are divided into four subgroups: supervised learning, unsupervised learning, semi-supervised learning, and reinforcement learning. In supervised learning models, datasets are used to train the algorithm and make predictions for new data inputs. By adjusting weights for each input as part of the cross-validation process, a system with high accuracy in prediction capabilities is developed.

During implementation, important parameters include linearity of the data, training time, prediction time, memory requirements, and analysis durations. It is generally necessary to start with simple models in the initial attempt. For example, evaluating results using linear models and decision trees, and if satisfactory accuracy is not achieved, more complex models such as neural networks, ensemble models, extreme gradient boosting, and support vector machines are tried. Therefore, in this study, linear regression and regression tree will be attempted for all three cases, followed by SVM and ANN methods. ML models will be created using data obtained from CFD results. In each case, the ML model will be trained using 70% of the dataset. The ML models are implemented using the MATLAB software.

4.1. Linear Regression (LR)

Linear regression finds the linear relationship between the dependent variable and one or more independent variables using a best-fit straight line. In general, a linear model makes predictions by simply calculating a weighted sum of the input features plus a bias term (also known as the intercept term). This technique is used in linear regression, where the dependent variable is continuous, and the independent variable(s) can be continuous or categorical, and the nature of the regression line is linear. Mathematically, the prediction using linear regression can be expressed as follows:

$$y(w,x) = w_o + w_1x_1 + w_2x_2 + \cdots + w_nx_n \quad (13)$$

Where y is the predicted value, n is the total of input features and x is the input feature. The main objective in linear regression is finding the best linear equation which predicts the output value based on the independent input values. Linear regression model has certain assumptions for its applicability. Firstly, a linear relationship between the independent and dependent variables is

expected. All the inputs should be independent variables. Homoscedasticity is required, meaning that the errors in the model are constant across all levels of the independent variables. The errors in the model are assumed to be normally distributed. There should be little to no correlation among the independent variables, or at worst, a very low degree of correlation. These assumptions limit the applicability of linear regression to problems that are predominantly nonlinear, such as fluid mechanics [43].

4.2. Random Forest (RF)

Random forest method which is an ensemble supervised algorithm uses random sampling of decision trees. The superior part of the RF is each of the tree in the RF model select features and samples, and in the final part final prediction is obtained by averaging of each of the tree. By that way, overfitting problem is avoided. Regression tree models increases the prediction accuracy by combining the regression trees. RF model has decision trees that investigates the subset of the input data. In Figure 15, the schematic of the RF model is illustrated.

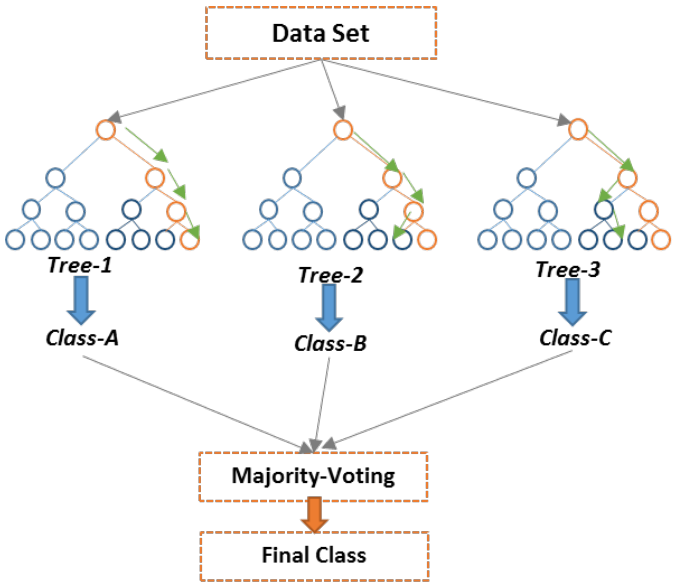

Figure 15. Process diagram of RF model

In the RF algorithm, each tree created depends on the values of a randomly sampled vector, independently. All trees have the same distribution. Instead of splitting each node by using the best partition among all variables, RF splits each node by using the best among a randomly selected subset of predictor variables for that node. The Eq. (14) shows the definition of the RF model that is educated with the tree number of k. In the equation $H(X, \theta_i)$ is the meta decision classifier. The

difference between meta decision tree classifiers and ordinary decision trees is that they do not directly predict the class value but rather indicate which base-level classifier to use for the prediction [44].

$$H(X,\theta_i) = \sum_{i=0}^{k} h_j\,(X,\theta_i), (i = 1,2,3,\ldots.,m) \tag{14}$$

4.3. Support Vector Machine (SVM)

The Support Vector Machine (SVM) method, like Artificial Neural Networks, is used for approximating multivariate functions with high precision. SVM performs exceptionally well in high-dimensional spaces and is a reliable approach for modeling nonlinear problems. The technique works by identifying a hyperplane that best divides a dataset into two classes. This hyperplane is selected by maximizing the margin between the classes, leading to an optimal solution. SVM is particularly effective in dealing with high-dimensional, nonlinear, noisy, and unstructured data, making it suitable for a wide range of applications. Additionally, SVM is computationally efficient, delivering globally optimal solutions with excellent consistency and repeatability. Figure 16 provides an example of SVM [45], [46].

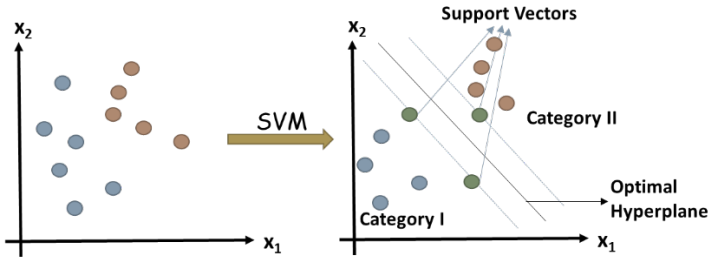

Figure 16. (a) Two classes (b) hyperplane that separated to two classes

4.4. Artificial Neural Network (ANN)

Neural Networks are comprised of a vast number of interconnected neurons organized sequentially. This array of neurons is known as layers, with the first layer being the input layer and the last layer being the output layer. ANNs are highly advantageous as they are able to learn the underlying patterns in a data set, enabling them to make accurate predictions and classifications. Furthermore, ANNs are highly adaptable and can be used to solve a wide range of problems. The input signals are transferred to the output layer from the input layer by passing the

hidden layer with using the activation functions and weights. The output of the ANN is expressed as follows:

$$y = p[f(W_1 x + B_1)W_2 + B_2] \quad (15)$$

In the equation p and f are the activation functions, W and B are the weights. ANN provides the output by characterizing the nonlinear correlation between the input and output parameters by the multi-layer neurons, activation functions and weight and bias vectors between neurons. The weight and bias vectors are determined by iterative learning process for each of the problem with using the numerical data for the current study. The artificial neural network architecture is depicted in Figure 17.

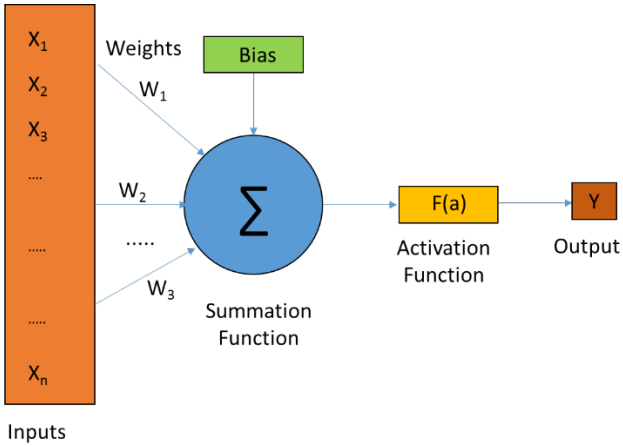

Figure 17. Structure diagram of artificial neural network model

As depicted in the figure, the input signals are weighted and added to the bias and connected to the activation function. In the final stage, the output data is generated in the output layer. The mathematical expression of this process is expressed in Eq (16).

$$y = \varphi\left(b + \sum_{i=1}^{n} x_i w_i\right) \quad (16)$$

In Eq (16), x_i is the input values, w_i denotes the weight, n is the number of data and φ is the activation function. In the training phase of the ANN structure forward propagation method is used as calculated follows:

$$M_j = \sum_{i=1}^{n} w_{ij} x_i + b_j \tag{17}$$

$$y_j = f(M_j) \tag{18}$$

4.5. Evaluation Of The ML Algorithms

For each case, the four ML methods with their defined mathematical frameworks will be applied. In order to compare the applied methods with each other and provide a numerical representation of which method offers what type of approach in which type of problem, the RMSE (Root Mean Square Error) and R (R-squared) statistical methods have been employed.

The R-value ranges from 0 to 1, with a higher value indicating increased accuracy. When R=1, it can be said that the used model provides perfect predictions. The mathematical representation of the Pearson correlation coefficient (R) is as follows:

$$R = \frac{\sum_{i=1}^{n}(x_i - \bar{x})(y_i - y)}{\sqrt{\sum_{i=1}^{n}(x_i - \bar{x})^2 \sum_{i=1}^{n}(y_i - y)^2}} \tag{19}$$

The RMSE value is utilized to demonstrate the percentage difference between the CFD data and the prediction data. A lower RMSE value indicates a better fit. The mathematical definition of RMSE is presented in the following equation:

$$RMSE = \sqrt{\frac{1}{N}\sum_{i=1}^{N}\left(\frac{R^e - R^p}{R^e}\right)^2} \tag{20}$$

By employing these statistical methods, the performance of each applied ML method can be compared, and the numerical representation of their respective approaches in different problem types can be presented.

5. MACHINE LEARNING RESULTS

For each of the data sets, sensitivity analysis is performed and hyperparameters are obtained and for the best scenario, results are depicted. In this part, firstly for each of the case ML results will

be given and then, a comparison of the ML results for each of the cases will be compared with each other. By this comparison, the type of problem and the type of technique that is the most powerful will be determined. For each of the cases, the input and output parameters are depicted in Figure 18, which also depicts the framework of the study.

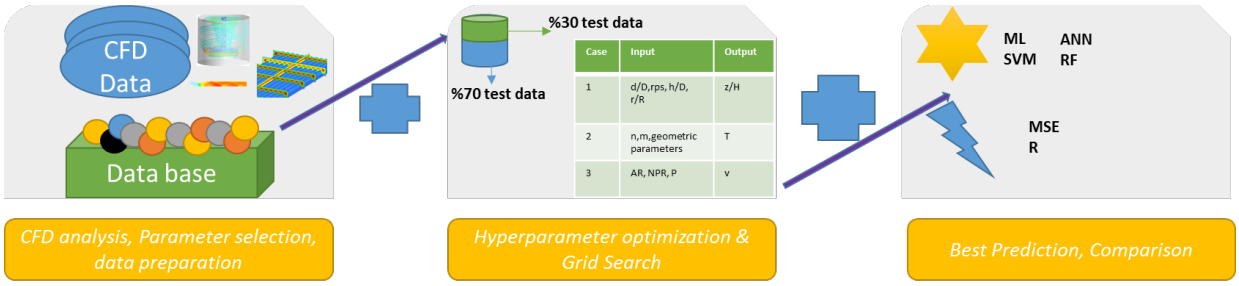

Figure 18. Framework of the study and Input and Output for ML

5.1. Linear Regression

In the linear regression model, the main objective is to find the best linear relationship between the dependent and independent variables. This is performed by obtaining the LR coefficients and measuring the difference between the numerical and predicted values. In the present study, the Stochastic Gradient Descent (SGD) algorithm is implemented to minimize the MSE. Independent variables and dependent variable(s) for each case are illustrated in Figure 19. For the SGD model, four types of regression model types are tried linear, interactions linear, robust linear, and stepwise linear model. In Figure 19, R values are given for each of the tried LR models for all of the cases. In the ML approach, the best approach was achieved for case 3 in all tested models. However, the R-squared values for all cases are below 0.8. The interactions linear model has provided the best approach among the three cases. This can be attributed to the ability of the model to capture complex relationships more effectively.

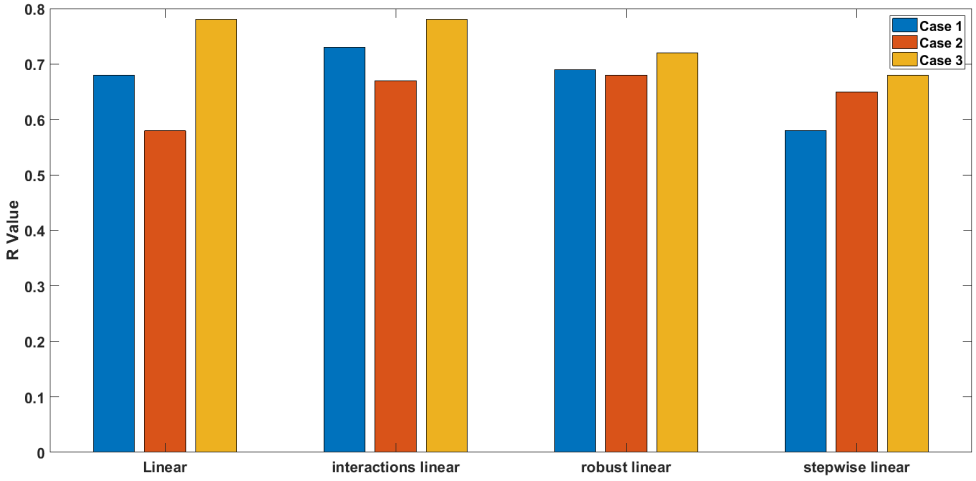

Figure 19. Pearson coefficient for four different LR models for each case

5.2. Support Vector Machine

In the analysis of SVM results for Case 1, it was found that the Cubic kernel delivered the poorest results, whereas the Gaussian kernel offered the most accurate predictions, as shown in Table 3. The number of box constraints had a relatively small effect, around 3.8%, when the kernel function was unchanged. However, the impact of the Box constraint became more noticeable when the kernel function changed, as seen in Fig 20. For example, with the Linear kernel, adjusting the *C* value from 5 to 25 only caused a 1.3% change in *R* and a 0.8% change in MSE. In contrast, when the *C* value was kept at five, but the kernel function shifted from Linear to Gaussian, *R* increased significantly by 19.7%, indicating a considerable performance improvement. The superior performance of the Gaussian kernel can be attributed to its ability to effectively capture nonlinear relationships, which is especially beneficial for modeling nonlinear problems.

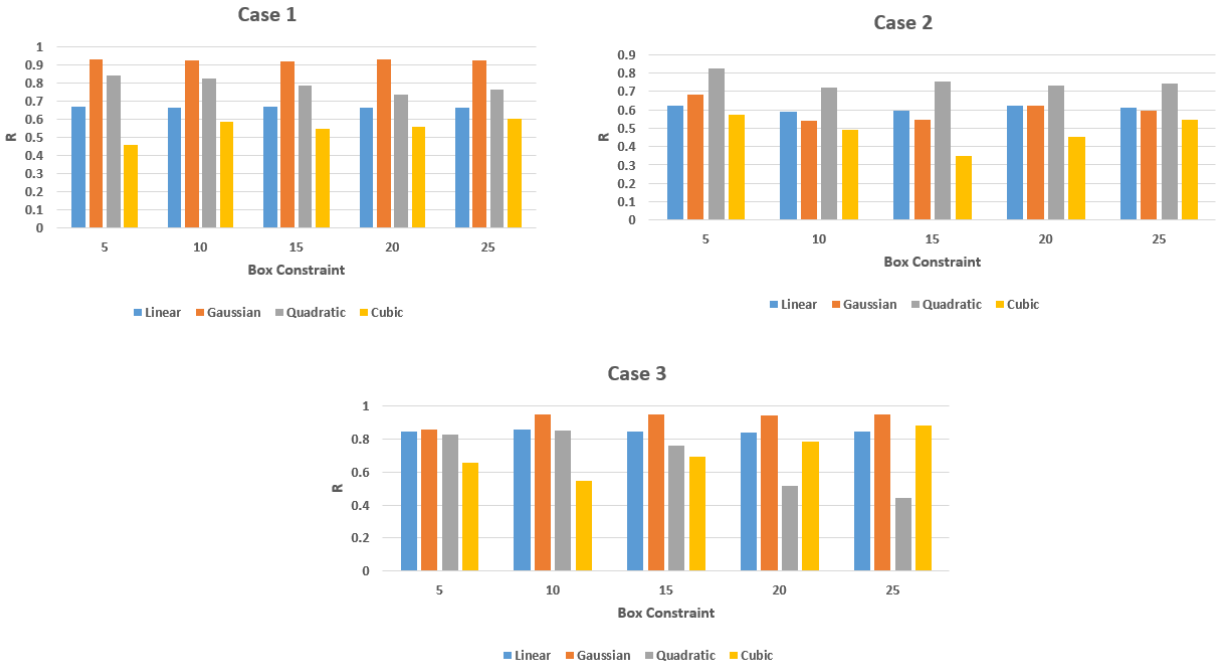

Figure 20. Effect of box constraint and different kernel functions

The impact of different kernel functions and box constraint values on various cases is illustrated in Figure 21. When using the linear kernel function, changing the value of c has minimal effect across all cases. On the other hand, when the cubic function is used, the impact of the box constraint value on R^2 reaches levels of up to 30%. In Case 1 and Case 3, the Gaussian kernel function maximizes the predictive performance, while in Case 2, the preferred function type is quadratic. According to the obtained results, it can be said that the choice of kernel function and C value should vary according to the nature of the problem, emphasizing the need for problem-specific determination.

Examining the impact of Kernel function variations on problem-solving time, the quadratic function performs approximately 2.2 times slower than the linear function in each problem. The longest solution time, regardless of the problem, is observed with the cubic function approximation, while the shortest solution times are achieved when using the linear function. Increasing or decreasing the box constraint value does not have a significant impact on computational cost.

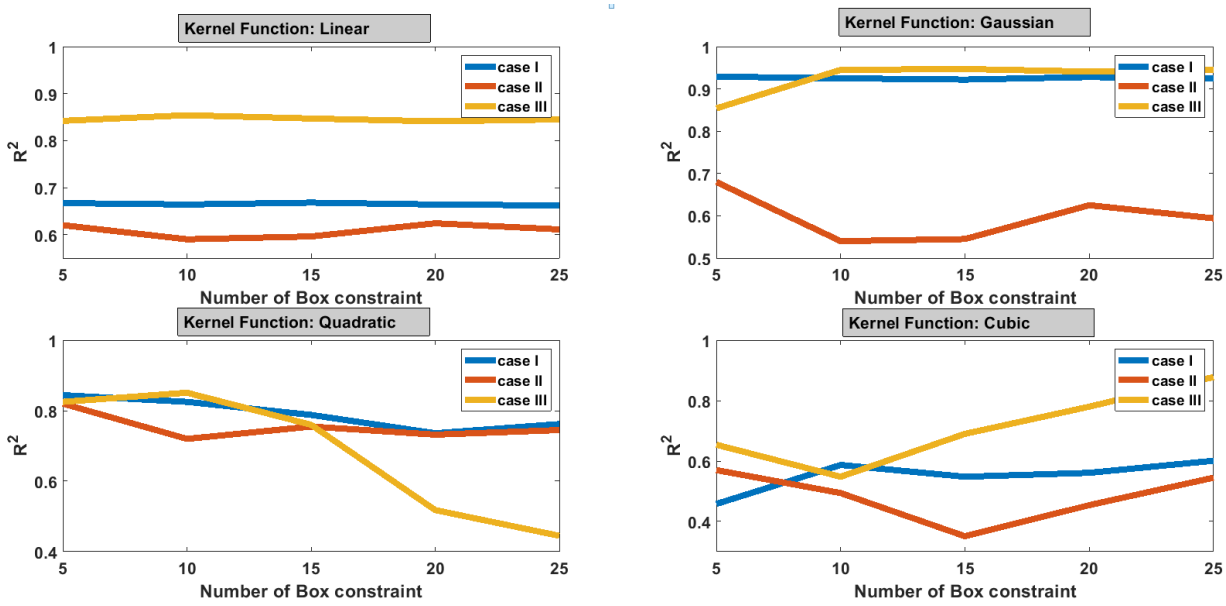

Figure 21. The effect of Kernel functions and box constraints on each case

5.3. Random Forest

For each of the cases, a trial-and-error test is utilized to optimize the number of leaf nodes and other parameters. In Table 3, the optimal values of hyperparameters for the RF model obtained by performing a grid search are given.

For each case, the impact of each parameter has been individually examined, leading to important findings. For example, in each case, as the number of estimators increases, the computation time also increases. When the number of estimators is increased by a factor of 10, the average computation time tends to triple. Increasing the number of estimators up to a certain point has improved the predictive power, but beyond a critical value, it starts to decrease. Therefore, it can be concluded that the number of estimators used in the Random Forest model has a critical value, where the predictive performance improves up to that value and declines afterward. However, it is important to note that this critical value may vary depending on the problem, making it a parameter that needs to be optimized for each specific problem.

Increasing the maximum depth helps the constructed trees to have a deeper understanding of more complex structures in the data. However, setting the maximum depth too high can lead to overfitting. Hence, it is another important parameter that needs to be optimized.

No linear relationship has been found between the depth and prediction ability. It has been determined that the optimal value for the maximum depth needs to be identified for each problem individually. Similarly, no linear relationship has been observed between the number of leaf nodes and prediction performance. In some problems, a higher number of leaf nodes resulted in higher R values, while in others, the opposite was observed. Table 3 provides the optimal values and corresponding R values for each case.

Table 3. Grid search results for RF

	Parameter	Searching Range	Optimal Value	R-value for optimal case
Case 1	Number of estimators	15,25,35,45,55,65,100,125,150	55	0.9978
	Maximum depth	20,30,40,50,60,80,100	30	
	Leaf nodes	10,15,20,25	15	
Case 2	Number of estimators	15,25,35,45,55,65,100,125,150	65	0.7854
	Maximum depth	20,30,40,50,60,80,100	40	
	Leaf nodes	10,15,20,25	15	
Case 3	Number of estimators	15,25,35,45,55,65,100,125,150	100	0.7248
	Maximum depth	20,30,40,50,60,80,100	30	
	Leaf nodes	10,15,20,25	25	

5.4. Artificial Neural Network

Artificial neural network architectures are defined as feedforward or backforward networks based on the connections between neurons. Feedforward networks do not have feedback connections, and each neuron in each layer transmits its output to the next layer through weights. In this study, the most commonly used feedforward network is the multilayer perceptron (MLP). Single-layer perceptrons can only solve linear problems, while multilayer perceptrons are often preferred for solving nonlinear problems [47].

In Case 1, as shown in Figure 20, there are four inputs and one output. In Case 2, there are three inputs and one output, and in Case 3, there are three inputs and one output. The outputs for Case 1-2-3 are *z/H*, temperature, and velocity, respectively. The number of neurons in the hidden layer will be determined through trial and error. Three different training algorithms, namely Bayesian Regularization, Scaled Conjugate Gradient, and Levenberg-Marquardt, were used. The hidden layer size was tested by varying it for each algorithm. Figure 22 illustrates the effect of the number of layers for different training algorithms. According to the results obtained, the training algorithm directly affects the model's performance. Additionally, the number of hidden layers in the model is another factor that affects its performance.

When examining the R^2 curves plotted for the test data, it can be observed that the highest R^2 values are achieved regardless of the training algorithm used in Case 3. This is believed to be due to the fact that Case 3 has the most data available. In Case 2, where the data is quite limited, the lowest R^2 values are obtained regardless of the algorithm and the number of hidden neurons. Consequently, it can be concluded that as the data size increases, the ANN architecture is better trained and provides better predictions. The SCG training algorithm has the highest computational cost for all three cases. As the number of hidden neurons increases, the solution time also increases, independent of the problem. In Case 1, the SCG model with 20 hidden neurons, in Case 2, the BLM model with three hidden neurons, and in Case 3, the BR model with 20 hidden neurons achieved the best predictions.

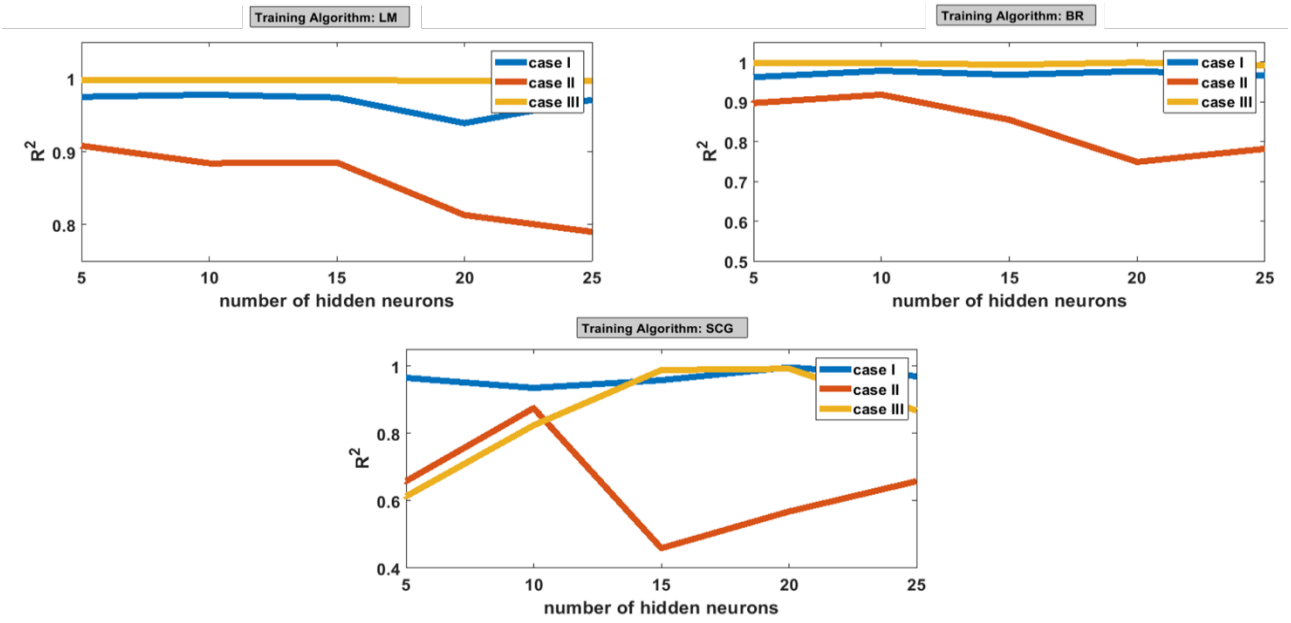

Figure 22. The effect of the training algorithm & number of hidden neurons in each case

5.5. Comparison of Machine Learning Results

In order to demonstrate the predictive capabilities of the four models tested for each specific problem, Figure 23 has been prepared. According to Kouvaras and Dhanak [48], a model with an R^2 value greater than 0.9 is considered to have high predictive ability. For Case 1, after optimizing the relevant parameters, the ANN, RF, and SVM models all have an R^2 value above 0.9. However, for Case 2, only the ANN method has been able to surpass this threshold. This can be attributed to the limited amount of available data. In Case 3, all models, except for LR, exhibit predictive abilities above the 0.9 threshold after conducting parameter optimization.

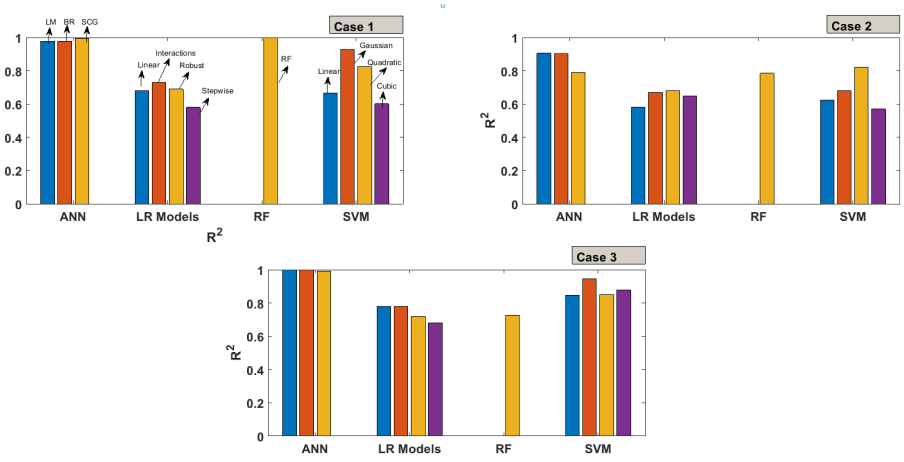

Figure 23. Comparison of R^2 values of all models for (a) Case-1, (b) Case-2, and (c) Case-3

In Figure 24, prediction values for each case are provided for the four models. The best architecture for each model has been selected, and the results obtained using that architecture are presented. For Case 1, the predicted parameter is the shape of the vortex. In stirrer flow, there are essentially two regions. The first region is referred to as the forced vortex zone, where the fluid behaves like a solid body, and the tangential velocity increases linearly with radius. The second region is the free vortex zone, where the tangential velocity undergoes a more complex change and drops to zero near the wall. When examining the predictive abilities of the ML models, it can be observed that all models accurately capture the shape of the vortex in the forced vortex zone. However, the predictive ability decreases in the free vortex zone. The ML-CFD model has the advantage of providing a single-phase solution, which saves time compared to CFD. With a sufficient amount of data, it is possible to say that ANN and RF models achieve high R^2 values and low error rates in such problems. However, it should be noted that the predictive ability decreases as the flow structure changes.

For Case 2, the temperature value is selected as the output. Case 2 has the smallest data size among the three cases. When looking at the results, the impact of data size on the efficiency of ML methods is clearly observed. A lower number of data points in the training set reduces the efficiency of the model. Having more data allows the model to encompass a wider data distribution and handle different scenarios. Therefore, the maximum R^2 value of 0.905 is found in the ANN method.

For Case 3, the velocity value is selected as the output. SVM and ANN methods have achieved high accuracy in prediction. On the other hand, LR and RF methods have shown lower prediction efficiency. Among the three cases, the ANN method has performed the best in terms of prediction. This is attributed to its ability to model complex systems through adaptive weight adjustments and process large data sets efficiently. SVM performs classification by using support vectors and can effectively determine complex boundaries. Indeed, SVM has provided high-accuracy results for all three cases. The LR model, being a linear model and assuming linear relationships between features, has not captured the relationships accurately for all three problems. In conclusion, each ML model provides different levels of accuracy for each data set, depending on factors such as linearity of the data, data size, relationships between the data, data distribution, and number of features. However, considering the context of fluid mechanics studies, it can be said that ANN, SVM and RF methods provide high accuracy in fluid mechanics problems.

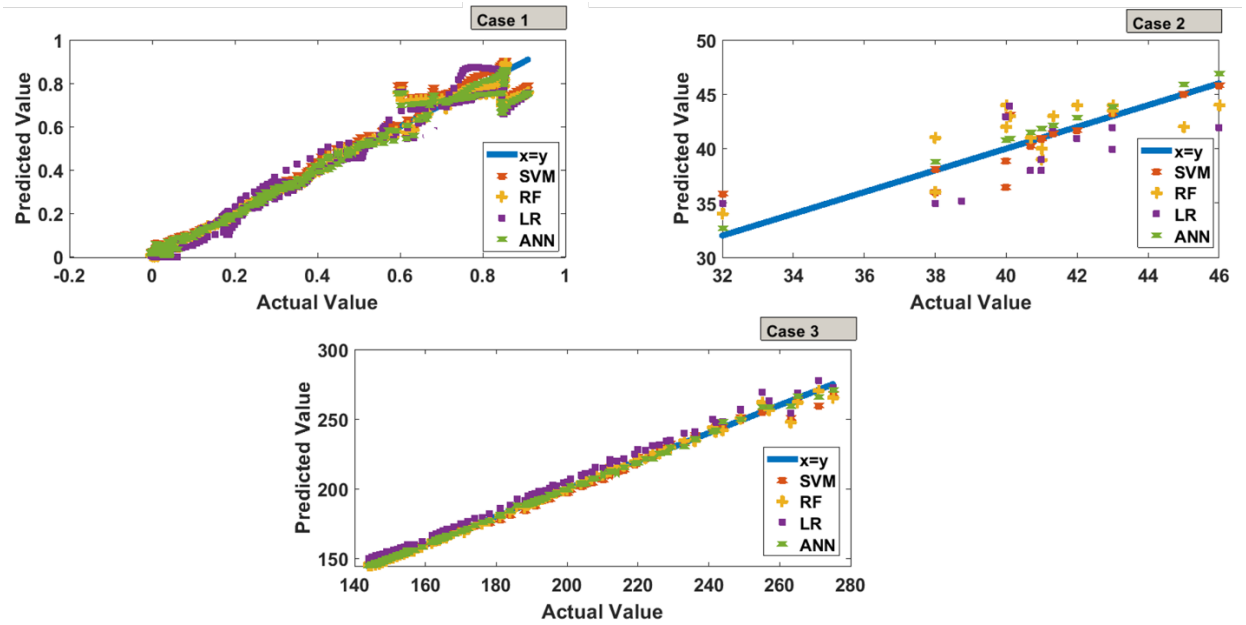

Figure 24. Prediction of (a) *z/H* for Case-1, (b) temperature for Case-2, and (c) velocity for Case-3 with different ML methods

6. DISCUSSION

The applicability of ML methods on three different fluid mechanics problems was investigated within the scope of this study. Firstly, the vortex mixer, solar air dryer, and converging-diverging nozzle problems were modeled using CFD. In the second stage, input and output parameters were determined for each case, and data were collected through numerical analyses. These data were used to explore the applicability of different ML methods on various fluid mechanics problems. The ML methods used in this study were Linear Regression, Random Forest, Support Vector Machine, and Artificial Neural Network. Optimization studies were conducted for each ML method in order to determine the most suitable architecture for each problem, and each model was developed to have the highest predictive capability for each specific problem. Although the main objective of this study was to test the effectiveness of ML methods, the numerical solutions to the fundamental fluid mechanics problems and the results that were obtained were presented in the study. The main results of the study can be summarized in two parts. The first part includes the CFD analyses, parametric analysis results, and the demonstration of flow phenomena for each case. The second part involves the effectiveness of ML methods for each case, their comparison with each other, and the comparison of the performance of the same method in different cases.

For the first part, each case study highlighted in detail the critical dependencies of performance and flow behavior on various parameters. In the case of the vortex mixer, variations in rotational speed and the d/D and h/D ratios had a significant impact on mixing efficiency. Specifically, the stirrer diameter notably influenced turbulence instabilities, particularly near the wall edges, while the initial water height exhibited limited effects on the central vortex dynamics.

For the solar air dryer, both mass flow rate and fin configurations played a substantial role in determining efficiency. However, as the mass flow rate increased, the enhancements in efficiency experienced diminishing returns. Finer fin spacing facilitated improved turbulence and enhanced heat transfer, contributing positively to the overall efficiency of the system.

Regarding the converging-diverging nozzle, modifications to the throat area ratio and nozzle pressure ratio demonstrated notable effects on flow characteristics such as velocity, volumetric flow rate, and temperature distribution. Specifically, higher AR values were associated with increased thrust generation, highlighting their influence on the overall performance of the nozzle.

In the second part of the study, different ML techniques were applied to each of the cases above, and the architecture of each ML method was optimized for each specific problem. The LR model was found to have the weakest predictive ability for each problem. The complex nature of fluid mechanics problems, often three-dimensional and turbulent, makes it challenging to establish linear relationships between flow parameters, and therefore, linear models such as LR do not appear to be well-suited for these types of problems. The accuracy of the SVM model is significantly influenced by the choice of the Kernel Function, which should be optimized for each problem to provide a better approach. For example, the Gaussian approach offers the best solution in Case 1, while in Case 2, this kernel function achieves average accuracy. Another parameter that has an impact on the SVM architecture is the Box Constraint value, and its variation affects the performance in each problem. However, compared to the influence of the kernel function, the effect of the Box Constraint is relatively low in all three problems. It was concluded that the Kernel Function is the most crucial parameter in the SVM architecture. Overall, the SVM method achieved high prediction accuracy after conducting the parametric analysis. When comparing with the RF method, different values for the number of estimators, maximum depth, and leaf nodes were tested through grid search over a wide range for each problem. The results showed that the RF model had an R^2 value of 0.9978 and a low MSE value for Case 1, while for the other two cases, the R^2 value remained below 0.7. Case 2 had only 30% of the data collected compared to the other two cases. Each ML method had the lowest predictive efficiency in Case 2, likely due to the limited data. The results indicate that ML methods require large datasets to improve prediction accuracy in fluid mechanics problems. Data quantity appears to be a parameter directly affecting the ML methods, and without sufficient data, no method can achieve the expected performance. When examining the impact of ANN methods, it was observed that the training algorithm had a dominant effect on performance and should be optimized for each problem.

Similarly, the number of hidden neurons was an influential parameter that caused different behaviors in the system for each problem. ANN was found to be the ML method with the highest predictive ability for each problem. Even in Case 2, which had a small data quantity, an R^2 value above 0.8 was achieved. The results indicate that each ML method exhibits different behaviors for each fluid mechanics problem, and some parameters need to be optimized for each ML method, which have varying effects on each problem. The LR method was found to have low applicability to fluid mechanics problems, while the SVM and ANN methods proved to be strong tools, especially after conducting the grid searches.

It should be noted that the limitation of this study is the reliance on CFD-generated data for training the ML models, which may not fully reflect the complexities of real-world conditions. Moreover, the need for large datasets to achieve high prediction accuracy remains a challenge in practical applications. Limited data, as observed in the solar air dryer case, prevents the predictive performance of ML methods.

7. CONCLUSION

The applicability of ML methods on three different fluid mechanics problems was investigated within the scope of this study. Firstly, the vortex mixer, solar air dryer, and converging-diverging nozzle problems were modeled using CFD. In the second stage, input and output parameters were determined for each case, and data were collected through numerical analyses. These data were used to explore the applicability of different ML methods on various fluid mechanics problems.

The key conclusions of this study are

- Linear regression methods showed limited applicability to fluid mechanics problems due to their inherent linear assumptions.
- Support vector machine and artificial neural methods exhibited strong predictive capabilities when optimized appropriately.
- Data quantity directly impacts the predictive accuracy of machine learning models, emphasizing the need for extensive datasets.
- Numerical data provided reliable training sources, but real-world validation remains necessary for broader applicability.

Recommendations for future studies are as follows:

- Validation of machine learning model predictions through experimental data to ensure improved real-world applicability.
- Enhancing data collection processes to increase dataset sizes, thereby improving the accuracy and generalizability of machine learning models.
- Investigating alternative machine learning methods or architectures that may be better suited to the unique complexities of fluid mechanics problems.

DECLARATION OF ETHICAL STANDARDS

The author of the paper submitted declares that nothing which is necessary for achieving the paper requires ethical committee and/or legal-special permissions.

CONFLICT OF INTEREST

There is no conflict of interest in this study.

CONTRIBUTION OF THE AUTHORS

Eyup Kocak: This study was conducted entirely by the author.

REFERENCES

[1] Camargo A, Muniz G, Duare B, Molle B. Applications of computational fluid dynamics in irrigation engineering. Rev. Ciência Agronômica 2020; 51(5): doi: 10.5935/1806-6690.20200097.

[2] Çengel Y, Cimbala JM. Fluid mechanics: Fundamentals and applications. 3rd ed. New York: McGraw-Hill Education; 2014.

[3] Rosenblatt F. The perceptron: A probabilistic model for information storage and organization in the brain. Psychol. Rev. 1958; 65(6): 386–408. doi: 10.1037/h0042519.

[4] Minsky M, Papert SA. Perceptrons: An introduction to computational geometry. Cambridge: The MIT Press; 2017.

[5] Hinton GE, Sejnowski TJ. Learning and relearning in Boltzmann machines. In: Rumelhart DE, McClelland JL, editors. Parallel distributed processing: Explorations in the microstructure of cognition. 1st ed. Cambridge: MIT Press; 1986. p. 282–317.

[6] LeCun Y, Bengio Y, Hinton G. Deep learning. Nature 2015; 521(7553): 436–444. doi: 10.1038/nature14539.

[7] Mehta UB, Kutler P. Computational aerodynamics and artificial intelligence. California 1984.

[8] Abd El-Aziz RM. Renewable power source energy consumption by hybrid machine learning model. Alexandria Eng. J. 2022; 61(12): 9447–9455. doi: 10.1016/j.aej.2022.03.019.

[9] Sakthi U, Anil Kumar T, Vimala Kumar K, Qamar S, Kumar Sharma G, Azeem A. Power grid-based renewable energy analysis by photovoltaic cell machine learning architecture in wind energy hybridization. Sustain. Energy Technol. Assessments 2023; 57: 103243. doi: 10.1016/j.seta.2023.103243.

[10] Tirth V, Algahtani A, Alghtani AH, Al-Mughanam T, Irshad K. Sustainable nanomaterial-based technologies for renewable energy production and efficient storage based on machine learning techniques. Sustain. Energy Technol. Assessments 2023; 56: 103085. doi: 10.1016/j.seta.2023.103085.

[11] Li Y, Yi YK. Optimal shape design using machine learning for wind energy and pressure. J. Build. Eng. 2023; 70: 106337. doi: 10.1016/j.jobe.2023.106337.

[12] Li J, Du X, Martins JRRA. Machine learning in aerodynamic shape optimization. Prog. Aerosp. Sci. 2022; 134: 100849. doi: 10.1016/j.paerosci.2022.100849.

[13] Zan BW, Ha ZH, Xu CZ, Liu MQ, Wang WZ. High-dimensional aerodynamic data modeling using a machine learning method based on a convolutional neural network. Adv. Aerodyn. 2022; 4(1): 39. doi: 10.1186/s42774-022-00128-8.

[14] Peng W, Zhang Y, Laurendeau E, Desmarais MC. Learning aerodynamics with neural network. Sci. Rep. 2022; 12(1): 6779. doi: 10.1038/s41598-022-10737-4.

[15] Khan A, Rajendran P, Sidhu JSS, Thanigaiarasu S, Raja V, Al-Mdallal Q. Convolutional neural network modeling and response surface analysis of compressible flow at sonic and supersonic Mach numbers. Alexandria Eng. J. 2023; 65: 997–1029. doi: 10.1016/j.aej.2022.10.006.

[16] Esrafilian-Najafabadi M, Haghighat F. Impact of occupancy prediction models on building HVAC control system performance: Application of machine learning techniques. Energy Build. 2022; 257: 111808. doi: 10.1016/j.enbuild.2021.111808.

[17] Ulucak O, Koçak E, Bayer O, Beldek U, Yapıcı EO, Aylı E. Developing and implementation of an optimization technique for solar chimney power plant with machine learning. J. Energy Resour. Technol. 2021; 143(5): doi: 10.1115/1.4050049.

[18] Aylı E, Koçak E. Supervised learning method for prediction of heat transfer characteristics of nanofluids. J. Mech. Sci. Technol. 2023; 37(5): 2687–2697. doi: 10.1007/s12206-023-0442-5.

[19] Aylı E, Koçak E. Prediction of the heat transfer performance of twisted tape inserts by using artificial neural networks. J. Mech. Sci. Technol. 2022; 36(9): 4849–4858. doi: 10.1007/s12206-022-0843-x.

[20] Aylı E. Modeling of mixed convection in an enclosure using multiple regression, artificial neural network, and adaptive neuro-fuzzy interface system models. Proc. Inst. Mech. Eng. Part C

J. Mech. Eng. Sci. 2020; 234(15): 3078–3093. doi: 10.1177/0954406220914330.

[21] Sim J, Mohan B, Badra J. Co-optimization of piston bowl and injector for light-duty GCI engine using CFD and ML. Fuel 2022; 329: 125455. doi: 10.1016/j.fuel.2022.125455.

[22] Aly AM, Clarke J. Wind design of solar panels for resilient and green communities: CFD with machine learning. Sustain. Cities Soc. 2023; 94: 104529. doi: 10.1016/j.scs.2023.104529.

[23] Ye Z, Hsu SC. Predicting real-time deformation of structure in fire using machine learning with CFD and FEM. Autom. Constr. 2022; 143: 104574. doi: 10.1016/j.autcon.2022.104574.

[24] Jin X, et al. Exploring the influence of nasal vestibule structure on nasal obstruction using CFD and machine learning method. Med. Eng. Phys. 2023; 117: 103988. doi: 10.1016/j.medengphy.2023.103988.

[25] Le DK, Guo M, Yoon JY. A hybrid CFD–deep learning methodology to improve the accuracy of cut-off diameter prediction in coarse-grid simulations for cyclone separators. SSRN Electron. J. 2022. doi: 10.2139/ssrn.4266592.

[26] Milićević A, et al. Effects of biomass particles size and shape on combustion process in the swirl-stabilized burner reactor: CFD and machine learning approach. Biomass and Bioenergy 2023; 174: 106817. doi: 10.1016/j.biombioe.2023.106817.

[27] Upadhyay M, Nagulapati VM, Lim H. Hybrid CFD-neural networks technique to predict circulating fluidized bed reactor riser hydrodynamics. J. Clean. Prod. 2022; 337: 130490. doi: 10.1016/j.jclepro.2022.130490.

[28] Nasution MKM, Elveny M, Syah R, Behroyan I, Babanezhad M. Numerical investigation of water forced convection inside a copper metal foam tube: Genetic algorithm (GA) based fuzzy inference system (GAFIS) contribution with CFD modeling. Int. J. Heat Mass Transf. 2022; 182: 122016. doi: 10.1016/j.ijheatmasstransfer.2021.122016.

[29] Mittal G, Kikugawa RI. Computational fluid dynamics simulation of a stirred tank reactor. Mater. Today Proc. 2021; 46: 11015–11019. doi: 10.1016/j.matpr.2021.02.102.

[30] Jia Z, Xu L, Duan X, Mao ZS, Zhang Q, Yang C. CFD simulation of flow and mixing characteristics in a stirred tank agitated by improved disc turbines. Chinese J. Chem. Eng. 2022; 50: 95–107. doi: 10.1016/j.cjche.2022.05.017.

[31] Li J, Deng B, Zhang B, Shen X, Kim CN. CFD simulation of an unbaffled stirred tank reactor driven by a magnetic rod: assessment of turbulence models. Water Sci. Technol. 2015; 72(8):

1308–1318. doi: 10.2166/wst.2015.314.

[32] Sarkar S, Singh KK, Suresh Kumar K, Sreekumar G, Shenoy KT. A novel ANN-CFD model for simulating flow in a vortex mixer. Chem. Eng. Sci. 2022; 260: 117819. doi: 10.1016/j.ces.2022.117819.

[33] Shoeibi S, Kargarsharifabad H, Mirjalily SAA, Zargarazad M. Performance analysis of finned photovoltaic/thermal solar air dryer with using a compound parabolic concentrator. Appl. Energy 2021; 304: 117778. doi: 10.1016/j.apenergy.2021.117778.

[34] Benhamza A, Boubekri A, Atia A, Hadibi T, Arıcı M. Drying uniformity analysis of an indirect solar dryer based on computational fluid dynamics and image processing. Sustain. Energy Technol. Assessments 2021; 47: 101466. doi: 10.1016/j.seta.2021.101466.

[35] Sileshi ST, Hassen AA, Adem KD. Simulation of mixed-mode solar dryer with vertical air distribution channel. Heliyon 2022; 8(11): e11898. doi: 10.1016/j.heliyon.2022.e11898.

[36] Chavan A, Vitankar V, Shinde N, Thorat B. CFD simulation of solar grain dryer. Dry. Technol. 2021; 39(8): 1101–1113. doi: 10.1080/07373937.2020.1863422.

[37] Singh R, Salhan P, Kumar A. CFD modelling and simulation of an indirect forced convection solar dryer. IOP Conf. Ser. Earth Environ. Sci. 2021; 795(1): 012008. doi: 10.1088/1755-1315/795/1/012008.

[38] Sudhakar P, Cheralathan M. Thermal performance enhancement of solar air collector using a novel V-groove absorber plate with pin-fins for drying agricultural products: an experimental study. J. Therm. Anal. Calorim. 2020; 140(5): 2397–2408. doi: 10.1007/s10973-019-08952-9.

[39] Karim MA, Hawlader MNA. Performance investigation of flat plate, v-corrugated and finned air collectors. Energy 2006; 31(4): 452–470. doi: 10.1016/j.energy.2005.03.007.

[40] Khan SA, Ibrahim OM, Aabid A. CFD analysis of compressible flows in a convergent-divergent nozzle. Mater. Today Proc. 2021; 46: 2835–2842. doi: 10.1016/j.matpr.2021.03.074.

[41] Subramani N, Sangeetha M, Gowtham G, Sai Kumar A. Flow and acoustic characteristics of convergent-divergent nozzle with and without wedges. Mater. Today Proc. 2023; Apr: 1-7. doi: 10.1016/j.matpr.2023.03.608.

[42] Mason ML, Putnam LE, Re RJ. Effect of throat contouring on two-dimensional converging-diverging nozzles at static conditions. 1980.

[43] Brunton SL. Applying machine learning to study fluid mechanics. Acta Mech. Sin. 2021;

37(12): 1718-1726. doi: 10.1007/s10409-021-01143-6.

[44] Todorovski L, Džeroski S. Combining classifiers with meta decision trees. Mach. Learn. 2003; 50(3): 223-249. doi: 10.1023/A:1021709817809.

[45] Zheng X, Schweickert R. Differentiating dreaming and waking reports with automatic text analysis and support vector machines. Conscious. Cogn. 2023; 107: 103439. doi: 10.1016/j.concog.2022.103439.

[46] Roy A, Chakraborty S. Support vector machine in structural reliability analysis: A review. Reliab. Eng. Syst. Saf. 2023; 233: 109126. doi: 10.1016/j.ress.2023.109126.

[47] Ataseven B. Yapay sinir ağları ile öngörü modellemesi. Öneri Derg. 2013; 10(39): 101-115.

[48] Kouvaras N, Dhanak MR. Machine learning based prediction of wave breaking over a fringing reef. Ocean Eng. 2018; 147: 181-194. doi: 10.1016/j.oceaneng.2017.10.005.